frontiers in Earth Science

ORIGINAL RESEARCH
published: 23 January 2019
doi: 10.3389/feart.2019.00001

Characteristics and Deposit Stratigraphy of Submarine-Erupted Silicic Ash, Havre Volcano, Kermadec Arc, New Zealand

Arran P. Murch[1], James D. L. White[1] and Rebecca J. Carey[2]*

[1] Department of Geology, University of Otago, Dunedin, New Zealand, [2] School of Physical Sciences, University of Tasmania, Hobart, TAS, Australia

Submarine eruptions dominate volcanism on Earth, but few are observed or even identified. Knowledge of how they operate is largely based on inference from ancient deposits, lagging by a decade or more our understanding of subaerial eruptions. In 2012, the largest wholly deep-subaqueous silicic eruption with any observational record occurred 700–1220 m below sea level at Havre volcano, Kermadec Arc, New Zealand. Pre- and post-eruption shipboard bathymetry surveys, acquisition by autonomous underwater vehicle of meter-scale-resolution bathymetry, and sampling by remote-operated vehicle revealed 14 seafloor lavas and three major seafloor clastic deposits. Here we analyze one of these clastic deposits, an Ash with Lapilli (AL) unit, which drapes the Havre caldera, and interpret the fragmentation and dispersal processes that produced it. Seafloor images of the unit reveal multiple subunits, all ash-dominated. Sampling destroyed layering in all but two samples, but by combining seafloor imagery with granulometry and componentry, we were able to determine the subunits' stratigraphy and spatial extents throughout the study area. Five subunits are distinguished; from the base these are Subunit 1, Subunit 2a, Subunit 3, Subunit 4 (comprising the coeval Subunit 4 west and Subunit 4 east), and Subunit 2b. The stratigraphic relationships of the four AL unit subunits to other seafloor products of the 2012 Havre eruption, coupled with the wealth of remote-operated vehicle observations and detailed AUV bathymetry, allow us to infer the overall order of events through the eruption. Ash formed by explosive fragmentation of a glassy vesicular magma and was dispersed by a buoyant thermal plume and dilute density currents from which Subunits 1 and 2 were deposited. Following a time break (days/weeks?), effusion of lava along the southern caldera rim led to additional ash generation; first by syn-extrusive ash venting, quenching, brecciation, and comminution (S3 and S4e) and then by gravitational collapse of a dome (S4w). Slow deposition of extremely fine ash sustained S2 deposition across the times of S3 and S4 emplacement, so that S2 ash was the last deposited. These thin ash deposits hold information critical for interpretation of the overall eruption, even though they are small in volume and bathymetrically unimpressive. Ash deposits formed during other submarine eruptions are similarly likely to offer new perspectives on associated lavas and coarse pumice beds, both modern and ancient, and on the

OPEN ACCESS

Edited by:
Nancy Riggs,
Northern Arizona University,
United States

Reviewed by:
Laura Pioli,
Università degli Studi di Cagliari, Italy
Katharine F. Bull,
Geological Survey of New South Wales (GSNSW), Australia

***Correspondence:**
James D. L. White
james.white@otago.ac.nz

Specialty section:
This article was submitted to Volcanology, a section of the journal Frontiers in Earth Science

Received: *16 June 2018*
Accepted: *04 January 2019*
Published: *23 January 2019*

Citation:
Murch AP, White JDL and Carey RJ (2019) Characteristics and Deposit Stratigraphy of Submarine-Erupted Silicic Ash, Havre Volcano, Kermadec Arc, New Zealand. Front. Earth Sci. 7:1. doi: 10.3389/feart.2019.00001

eruptions that formed them. Submarine ash is widely dispersed prior to deposition, and tuff is likely to be the first product of eruption identified in reconnaissance exploration; it is the start of the trail to vent hydrothermal systems and associated mineralized deposits of submarine volcanoes, as well as a sensitive indicator of submarine eruptive processes.

Keywords: submarine, Havre volcano, seafloor ash, fragmentation, stratigraphy, pyroclastic eruption

INTRODUCTION

Eruption into a deep subaqueous environment is complex. In addition to influences of magma composition and rheology (Walker and Croasdale, 1971; Dingwell and Webb, 1990), volatile content of the magma, and magma flux (Gonnermann and Manga, 2003; Namiki and Manga, 2008), submarine eruptions are significantly modulated by the physical properties of water, both indirectly (hydrostatic pressure, increased viscosity of water relative to air) and directly (rapid heat transfer, rapid volume expansion of vaporized seawater) (Head and Wilson, 2003; White et al., 2003, 2015; Cas and Giordano, 2014). Hydrostatic pressure will suppress the magnitude of volatile exsolution and expansion, and is presumed to limit explosive expansion and related fragmentation (Fisher, 1984; Staudigel and Schmincke, 1984). Rapid heat transfer on direct contact between magma and water, however, can induce both explosive (Zimanowski et al., 1997; Austin-Erickson et al., 2008) and passive fragmentation (Carlisle, 1963; Kokelaar, 1986; Schmid et al., 2010; van Otterloo et al., 2015).

The cost and difficulty of collecting seafloor samples that can be linked directly to subaqueous eruptive dynamics, and the complexity of modeling these processes (both physically and computationally), has led to diverse interpretations of eruptive processes in the subaqueous environment (Head and Wilson, 2003; Allen and McPhie, 2009; Schipper et al., 2010; Rotella et al., 2013; White and Valentine, 2016). Much of our understanding comes from studies of uplifted subaqueous volcanic successions (e.g., Cas, 1978; Dimroth and Demarcke, 1978; Staudigel and Schmincke, 1984; Busby-Spera, 1986; Dimroth and Yamagishi, 1987; Kano et al., 1996; Allen and McPhie, 2000; Simpson and McPhie, 2001; Allen and Stewart, 2003; Cas et al., 2003; Stewart and McPhie, 2004; Allen and McPhie, 2009; Jutzeler et al., 2015).

In this paper, we present observations and data on a proximal seafloor ash deposit called the Ash with Lapilli unit (AL unit), sampled 3 years after the deep submarine eruption of Havre volcano (Carey et al., 2014, 2018; Manga et al., 2018; Mitchell et al., 2018). Sampling and observations by remote-operated vehicle (ROV) Jason, guided by high-resolution bathymetry from the autonomous underwater vehicle (AUV) Sentry (Carey et al., 2018), show that the AL unit contains different layers of ash formed during the eruption. The differing distributions of the AL unit ash layers, together with textural differences among deposits and their ash particles, allow us to interpret their origins during the eruption sequence. The study of the AL deposit provides a vital stratigraphic framework for the eruption allowing us to interpret the temporal evolution in processes of the largest known historic wholly deep-subaqueous (>0.5 km; well below wave base) silicic eruption.

GEOLOGICAL SETTING

Havre is a seamount volcano first described by Wright et al. (2006), located at 31° 05′S 179° 5′W (−31.10, −179.03) along the Kermadec arc (**Figure 1a**). The edifice rises from 1500–2000 m below sea level (mbsl) to a peak along the caldera wall at 600 mbsl. The caldera is 4 km long and 3 km wide, elongate northwest–southeast, and has an average caldera-rim depth of 900 m. The caldera floor is at 1500 mbsl (**Figure 1b**).

Havre volcano erupted most recently in 2012 (Carey et al., 2014, 2018; Jutzeler et al., 2014). Satellite images acquired at 1050 18 July 2012 UTC (universal coordinated time; all subsequent times in UTC) show an eruption plume and hot spot emanating from a point source above Havre (**Figure 1a**). An image taken 11 h later at 2151 shows a 400 km^2 pumice raft. Satellite imagery indicates that eruptive activity affecting the sea-surface, including origination of the atmospheric plume, pumice raft, and of a plume of discolored, ash-stained, water, extended over 21.5 h. An image taken at 0209 20 July 2012 shows the pumice raft detached from its source and no atmospheric plume, indicating the eruption was no longer powerful enough to produce effects at the sea surface. From 17 to 21 July frequent earthquakes of magnitude 3–5 were also recorded from Havre. After 21 July 2012, there is no record in satellite imagery or recorded seismicity of further activity at Havre.

Comparison of shipboard bathymetry surveys conducted in 2002 (Wright et al., 2006) and after the eruption, on 26 October 2012, revealed substantial topographic changes on the volcano (Carey et al., 2014, 2018). Several dome/cone shaped features had been produced on the southern caldera rim along with a large "bulge" on the southwest caldera wall. The seafloor products of the Havre eruption were subsequently mapped at high resolution, imaged, and sampled in a 2015 cruise using AUV Sentry and ROV Jason (**Figure 1b**). Fifteen domes and lavas were erupted (A–P) along the southern and southwestern caldera rim (**Figure 1b**; Carey et al., 2018). Three clastic units were mapped on the seafloor. The lowest observed stratigraphic unit is a widespread deposit composed of giant pumice clasts >1 m in diameter [Giant Pumice unit (GP unit)] extending and coarsening to the NW and inferred to predate Dome OP in the southwest. No clear exposures were found of the contact between GP unit and the pre-2012 substrate, but observations on caldera walls and rims indicate that no other deposits of significant thickness there underlie the GP unit. Surrounding Dome OP is a local unit with lobate distribution, the Ash, Lapilli, and Block unit (ALB unit). The ALB unit overlies, and near the dome buries, the GP unit, with several lobes extending from Dome OP onto the caldera rim and into the caldera. The AL unit, which over most of its extent consists almost entirely of ash, is the most widespread unit, found

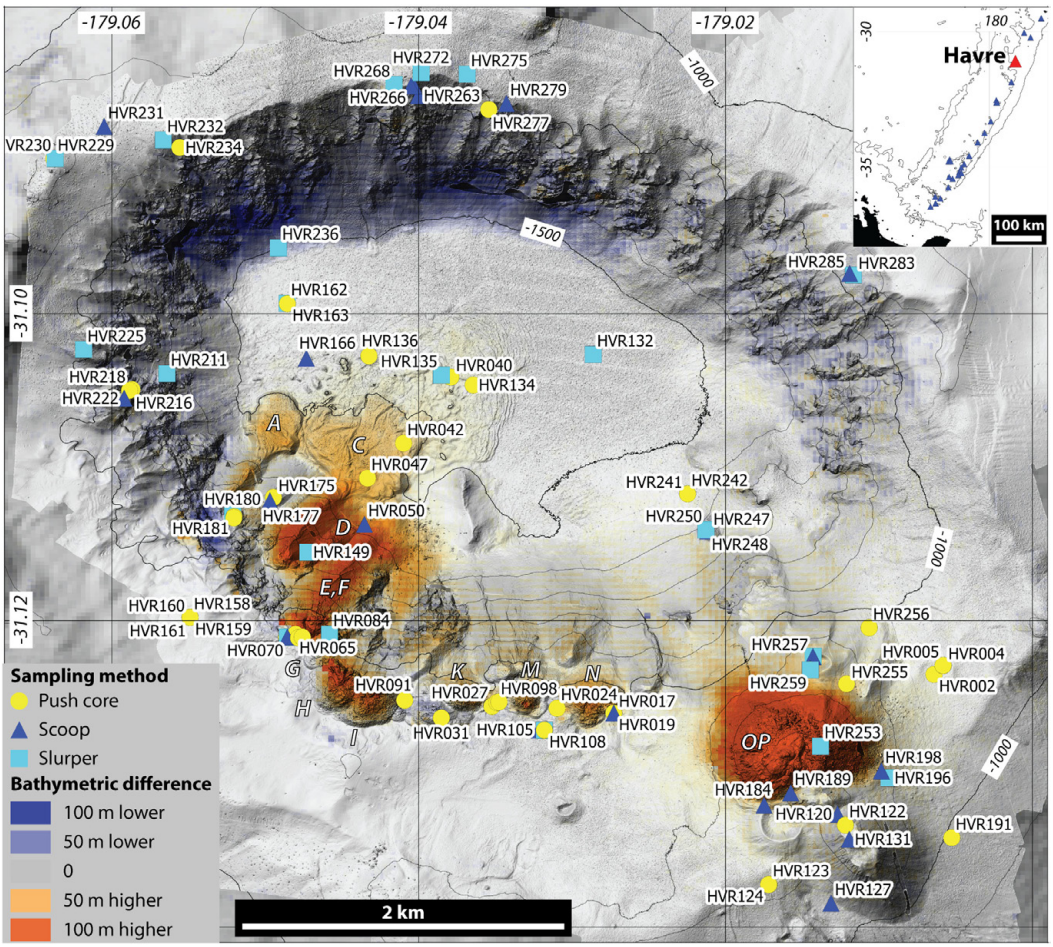

FIGURE 1 | A bathymetry map of the Havre caldera and summit with meter-scale resolution, overlain on a lower resolution (35 m) bathymetry map of the region. Overlay shows the bathymetry differences between the 2002 and Oct 2012 surveys (orange = material added, blue = material removed). The locations of all clastic samples taken at Havre are shown along with the sampling method used. Insert shows the location of Havre seamount (red) along the Kermadec arc.

in every location visited by the ROV. The AL unit overlies the GP unit and is composed of four subunits, the upper three of which also overlie the ALB unit; the relationship of the basal subunit of the AL unit to the ALB unit is not known. Since the basal contact of the GP unit was not observed in detail it is not known whether the AL unit represents the earliest ash deposit from the eruption, or whether further thin ash deposits underlie the GP unit. The AL unit has a combined volume of <0.1 km^3 (Carey et al., 2018) and is the focus of the present study.

The magma erupted at Havre in 2012 shows a rhyolitic whole-rock composition with little variation between the various clastic units and lavas (Carey et al., 2018).

MATERIALS AND METHODS

Ninety-two samples were taken from the caldera floor, walls, and rims (**Figure 1**) using ROV Jason and employing push-cores, scoops, and vacuum-like "slurp" samplers. The samples used in this study and the methods by which they were collected are summarized in **Supplementary Table 1**, with details of the sampling devices provided in **Supplement 1.1**.

All sampling methods were generally destructive of deposit layering and returned a mixture of particles from the clastic units sampled. There is no discernible difference in the grainsize characteristics of samples taken by different methods (push core, scoop, and vacuum).

All samples were immediately dried either in an oven at 90°C or under an array of heat lamps for at least 8 h. Whole samples were hand sieved onshore, from −4 φ to 4 φ (from 16 to 0.063 mm) in ½ φ steps. The fraction remaining in each sieve was weighed to 0.01-g resolution. Particles smaller than 0 φ (1 mm) were also analyzed in a Mastersizer 2000® laser analyzer (at least three runs per sample). Merging of the sieving and Mastersizer curves was undertaken on a sample by sample basis, with the point overlap chosen to produce the most realistic grainsize distribution and avoid anomalies induced by adherence and aggregation of fine to extremely fine ash during sieving. The chosen overlap point was generally around 0.5 φ (0.71 mm). Merging was undertaken by scaling the re-binned Mastersizer®

data to the fraction of the sieved sample below the chosen point [i.e., if 20% of the sieved sample was less than 1 φ (the chosen merge point) then the Mastersizer® data were rescaled to reflect its wt% in the whole sample]. The chosen point produced the lowest difference from 100 wt% when adding the sieving and Mastersizer® data.

Componentry was conducted at whole φ steps on material from −2 to 2 φ (4 mm to 125 μm). For larger particles, −2 φ to 0 φ (4–1 mm), categorization and identification were done with the naked eye and for 1 φ and 2 φ (500–250 μm) fractions, by binocular microscope. For each size fraction, at least 300 grains were analyzed as sample splits or entire samples. Three first-order juvenile component groups were identified based on grain color and morphology. These first-order groups were then subdivided into several second-order subgroups defined on surface morphology and texture. Grain counts of SEM-SE-imaged populations (see below) were also made for particle size fractions 3 φ (125 μm), 4 φ (63 μm), and smaller than 4 φ.

Grain morphology and microtextures were investigated using secondary electron (SE) and back-scattered electron (BSE) methods on a Zeiss Sigma VP® Field-Emission-Gun scanning electron microscope (SEM) at the University of Otago. For SE (morphological) imaging, grains were mounted on an SEM stub using carbon tape and then carbon coated. BSE imaging was undertaken on sectioned grains mounted in a carbon-coated polished briquette. In both cases, imaging was undertaken using a 15-keV accelerating voltage and a working distance of between 7.1 and 9.5 mm.

RESULTS

Identification of Strata Within the AL Unit

Seafloor observations did not reveal natural vertical exposures through the AL unit, but layering was observed in incisions (**Figures 2a–d**) produced by sampling at several sites (HVR042, HVR132, HVR163, HVR196, HVR229, HVR232, and HVR272). In addition, two push cores (HVR159 and HVR134) preserved distinct layers. By combining observations of the seafloor (e.g., 2e–k) and preserved samples, four distinct layers are identified in the AL unit.

Four layers were observed at sites HVR132 and HVR163 (**Figures 2a,b**) and had similar characteristics and thicknesses at each. Two layers were observed at site HVR196 (**Figure 2c**), and a single layer at sites HVR229, HVR232, and HVR272. In each case, the observed layers displayed similar characteristics and thicknesses to one of the layers observed at HVR132 and HVR163 (**Figure 2d**). Detailed observation descriptions of each site are presented in **Supplement 1.2**.

Pushcore HVR159 is the most important single AL sample. It is from the southwest caldera rim and was taken through a thick deposit of the AL unit, beyond the boundary of the GP unit and away from any significant slopes. Here the push core sampled and preserved at least four layers, the upper three of which were visible (**Supplementary Figure 2**). The basal part of the sample, which mostly collapsed when removed from the push core, was a light-colored layer between 4 and 5 cm thick composed of fine to coarse ash. Stratigraphically overlying this layer was a 1 cm-thick layer rich in elongate coarse ash grains. Next, above a sharp basal contact, was a 2.5 cm-thick dark-colored, medium-to-coarse-ash layer. The uppermost layer was cohesive and 2 cm thick.

Pushcore HVR134 was taken on the caldera floor, northeast of Lava C through a thick deposit of the AL unit near the base of a slight slope, in an area with hummocky topography (**Figure 1b**). The push core shows only two layers: a basal gray cohesive fine-grained layer ∼20 cm thick, overlain by a dark gray layer 8 cm thick.

Remote-operated vehicle images of the AL unit overlying 2012 Havre lavas show reduced deposit coverage and thickness compared with AL deposits on older lavas of similar morphology. Atop pre-2012 lavas on the southern caldera rim the AL unit is consistently thick (**Figures 2g,h**). In contrast, the AL unit overlying Lavas H, I, K, M, and OP (**Figures 2i–k**) comprises thin patchy deposits. Across Lava N a sharp divide in deposit coverage is observed. Most of Lava G has GP clasts on it and a thick, consistent mantling AL deposit, but the central part of Lava G shows only a thin, patchy AL deposit.

Granulometry and Componentry of HVR134 and HVR159

A critically useful feature of the two samples that did preserve layering (HVR134 and HVR159) is that particles making up the layers have distinctive characteristics. Both HVR134 and HVR159 pushcores were subsampled on the ship from their basal and top layers. The material that remained after removal of the subsamples formed a mixed sample containing material from both subsampled layers and the remainder of the sample. In HVR159, two additional layers are visible in the middle of the sample which were not separately subsampled. Granulometry and componentry were conducted on both the mixed samples and the basal- and top-layer subsamples of HVR134 and HVR159 and reveal common layer-particle characteristics.

Granulometry of mixed samples from HVR134 and HVR159 shows two main grain size peaks, determined using GRADISTATv8 (Blott and Pye, 2001). A 6–5 φ (16–32 μm) fraction dominates HVR134, and one of 2–1 φ (250–500 μm) is dominant in HVR159, with a minor peak between 0 and −1.5 φ (1–2.8 mm) (**Figure 3**). In both samples, the basal layer subsample displays a bimodal grain size distribution with modes at 2–1 φ and 0 to −1.5 φ (**Figure 3**). The top layer subsample of both HVR134 and HVR159 displays a unimodal distribution with a mode of extremely fine ash (White and Houghton, 2006) at 6–5 φ. We used the granulometry modes in mixed samples taken from around the caldera to map the distribution of specific layers.

Componentry was conducted in 1 φ steps from −2 to 2 φ (4 mm to 250 μm) for 27 samples. Grains were counted into three first-order groups: glassy vesicular, microcrystalline, and elongate tube-vesicle particles (**Figure 3c**). These first-order groups are subdivided into secondary classes based on particle vesicularity and morphology (**Figure 3c**). No lithic component was recognized in any sample examined.

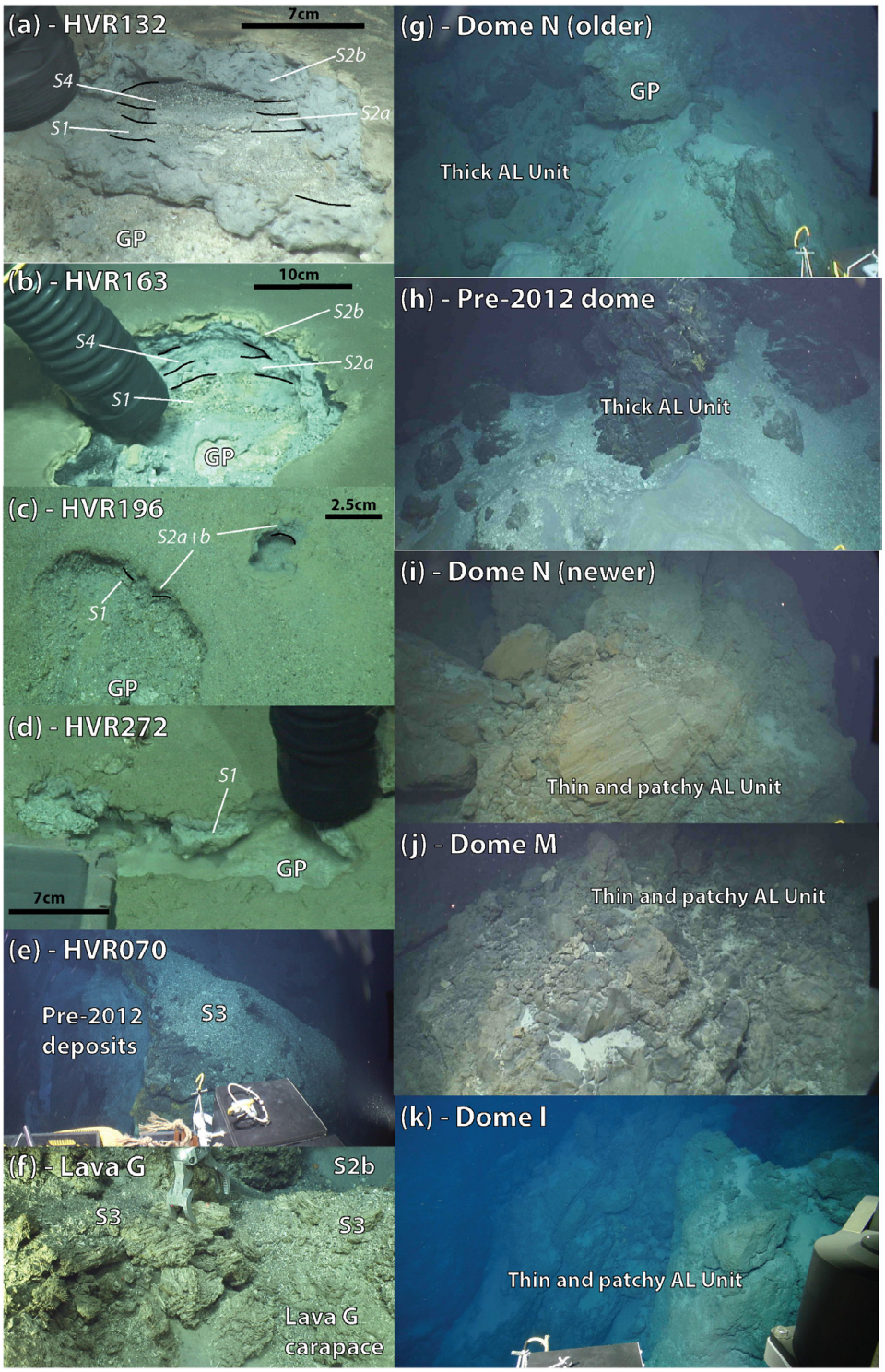

FIGURE 2 | Seafloor images of AL unit layering exposed during sampling from atop GPs at locations HVR132 **(a)**, HVR163 **(b)**, HVR196 **(c)**, and HVR272 **(d)**. At both HVR132 **(a)** and HVR163 **(b)** a similar stratigraphy can be observed showing four layers with comparable layer thicknesses, apparent grainsize, and color. At HVR196 **(c)** only two layers can be seen. At HVR272 **(c)** only a single layer can be seen (**e** and **f**) show a clastic deposit consisting of lapilli and ash with dominantly elongate tube morphologies at HVR070 **(e)** and overlying the carapace of Lava G **(f)**. In **(g–k)**, the variation in the AL unit coverage overlying lavas around the caldera is shown. Thick deposits of the AL unit can be seen overlying an apparently older part of Lava N **(g)** and also overlying a lava produced prior to the 2012 Havre eruption **(h)**. Over the more-recent part of Dome N **(i)**, and on Domes M **(j)**, and I **(k)**, the AL unit is thinner and patchier. Domes with similar shapes were chosen to provide a consistent context for observed variations in the AL unit.

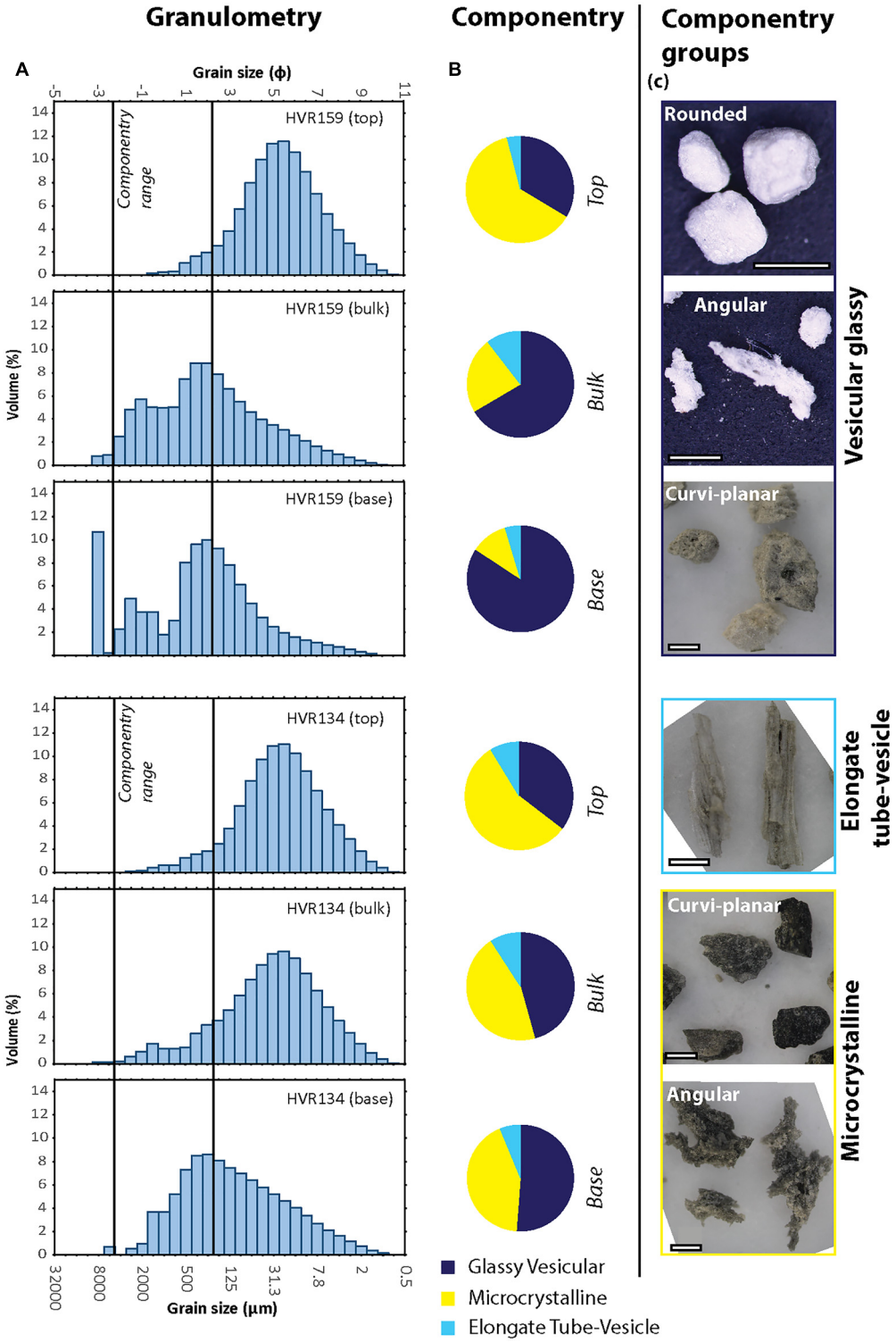

FIGURE 3 | Grainsize distribution **(a)** and componentry **(b)** for samples HVR159 mixed, HVR134 mixed, and their basal and upper layer subsamples. The upper sub-sample is finer grained, shows a decrease in glassy vesicular particles, and a concurrent increase in microcrystalline particles from its bottom to top. In the mixed sample, there is a concentration of elongate tube-vesicle particles. Componentry range indicated for both samples. Small subsamples removed from mixed samples (<5% mixed-sample mass) slightly reduce measured proportions of subsampled ash in mixed samples. **(c)** Optical images that show the componentry classes and their morphological subclasses. Color differences in particles are due to groundmass microcrystallinity, where microcrystalline particles show a higher crystallinity than glassy vesicular, and elongate tube-vesicle particles.

Glassy vesicular grains are white to creamy gray glass of moderate to high vesicularity (**Figure 3c**). Microcrystalline grains are black to dark gray, microcrystalline, and weakly to non-vesicular (**Figure 3c**). Elongate tube-vesicle clasts are white to cream-colored glass with elongate shapes defined by tube vesicles; they have a woody/fibrous appearance (**Figure 3c**).

Componentry of individual layers preserved in the HVR159 and HVR134 was used in parallel with granulometry (**Figure 3**) to determine layer distributions. In HVR159, there is an increase in the proportion of microcrystalline clasts from 11% in the basal layer subsample, to 23% in the mixed sample and 62% in the top layer subsample. Glassy vesicular clasts decrease from 83% in the basal layer to 66% in the mixed sample, to 25% in the top layer. The broad trend of increasing microcrystalline clasts and decreasing glassy vesicular clasts from the base to the top of the AL unit is repeated in sample HVR134, with microcrystalline clasts comprising 42%, 45%, and 54% of the basal layer, mixed sample, and top layer, respectively. The mixed sample of HVR159 also shows the highest percentage of elongate tube-vesicle clasts, 10% compared to 5% and 4% in the basal layer and top layer, respectively (**Figure 3**).

Nomenclature and Stratigraphy of Layers Within the AL Unit

Seafloor observations, plus granulometry and componentry from preserved stratigraphy in push cores, indicate that there are four subunits within the AL unit.

Subunit 1 (*S1*) – The basal layer in seafloor images of the AL unit and in sample HVR159 is a >6-cm-thick, light-cream-colored deposit of coarse ash (**Figures 2a–c**, **3**). We identify grainsize modes at 2–1 φ and 0 to −1.5 φ (the large mode is subdued) (**Figure 3**). Overall S1 is dominated by glassy vesicular clasts. Subunit 1 is also shown in seafloor images at HVR132 and HVR163 to directly overlie the GP unit.

Subunit 2 (*S2*) – Subunit 2 was observed on the seafloor as a cohesive extremely fine ash and has a measured modal grainsize of 6–5 φ. It overlies S1 across a gradational contact (**Figures 2a–c** and **Supplementary Figure 1**). The fine modal grainsize of particles in S2 precluded standard componentry, but they were examined by SEM (see below). Observations from HVR132 and HVR163 show that Subunit 2 is locally divided into lower (a) and upper (b) where separated by subunits 3 and 4 (**Figure 6**). Elsewhere S2 is a single layer without any visible internal contact(s). Subunit 2a was observed at sites HVR132 and HVR163 (**Figures 2e,f**) where it is approximately 2 cm thick (**Figures 2e,f**, **6**). Subunit 2b is 4–10 cm thick on the caldera floor and 2–3 cm thick on the southern, eastern, and western caldera rims. Subunit 2 particles are characterized by their consistent 6–5 φ modal grainsize.

Subunit 3 (*S3*) – Push core HVR159 has in its midsection an approximately 3 cm thick layer rich in elongate clasts. Subunit 3 is dominated by elongate tube-vesicle clasts. It overlies Subunit layer 2a.

Subunit 4 (*S4*) – This subunit is 2 cm thick and composed of medium/coarse dark colored ash at seafloor locations HVR132 and HVR163 (**Figures 2a,b**), and in push core HVR159. Subunit 4 directly overlies S3 across a sharp boundary. The granulometry of S4 is uncertain because it was not directly sampled, but comparison of the characteristics observed in push core HVR159 with identified components indicates that Subunit 4 is dominated by microcrystalline particles.

Mapping Subunits Using "Mixed" Samples

Observed seafloor stratigraphy at HVR132, HVR163, and granulometry and componentry characteristics of subunits from push core HVR159 allow us to establish the presence or absence of subunits in the other, mixed, samples where no layering was preserved. For example, the presence of the 6–5 φ grain size mode indicates the presence of Subunit 2. By establishing the presence of subunits in mixed samples, we can map the distribution of the subunits across the study area. For our sampling locations, the proportional depth of sampling within the overall deposit is unknown, so deeper layers may not have been sampled or have been under-sampled. This limitation would most strongly affect the mapped distribution of S1 (the basal layer). Subunit 1 was, however, identified in all samples, apart from a few taken on steep slopes and on lavas on the southern caldera rim, indicating that samples acquired contain the full sequence.

Granulometry of 81 mixed samples of the AL unit shows that they are composed of >90% ash with complex multi-modal grainsize distributions. The grainsize distributions are unimodal and bimodal, with common modes identified at 6–5 φ (16–32 μm) associated with Subunit 2, and between 3.5 and 0.25 φ (88–840 μm) associated with Subunit 1 (**Figure 4**). Seven ash-dominated samples also show grainsize modes in the 0 to −2 φ (1–4 mm) range. The presence of subunits inferred from granulometry was confirmed by componentry showing the presence of particle types also characteristic of the subunits (see the section "Nomenclature and Stratigraphy of Layers Within the AL Unit," **Figure 5**). Subunit characteristics are summarized in **Table 1**.

Subunit 1

Seafloor images show S1 thicknesses of 2–6 cm (**Figures 2a–c**, **6**). Common seafloor ripples and strong seafloor currents encountered during *ROV Jason* dives suggest deposit reworking, so observed layers may not preserve their original thicknesses. The glassy vesicular clasts that characterize S1 have been identified in all clastic samples, indicating that S1 extends across all the study area and beyond it (**Figure 5**). The grainsize mode of S1 in pushcore HVR159 is 2–1 φ (0.25–0.5 mm). The mixed samples show a regular fining of the coarser grain size mode from 0 φ (1000 μm) near dome OP, toward 3.5 φ (88 μm) to the WNW on the far caldera rim (**Figure 4**).

Subunit 2

Subunit 2 is locally divided into lower (a) and upper (b) where separated by Subunits 3 and/or 4 (**Figure 6**). Elsewhere Subunit 2 is a single layer without any visible internal contact(s). Subunit 2a was observed at sites HVR132 and HVR163 (**Figures 2e,f**) where it is approximately 2 cm thick (**Figures 2e,f**, **6**). Subunit 2b is 4–10 cm thick on the caldera floor and 2–3 cm thick

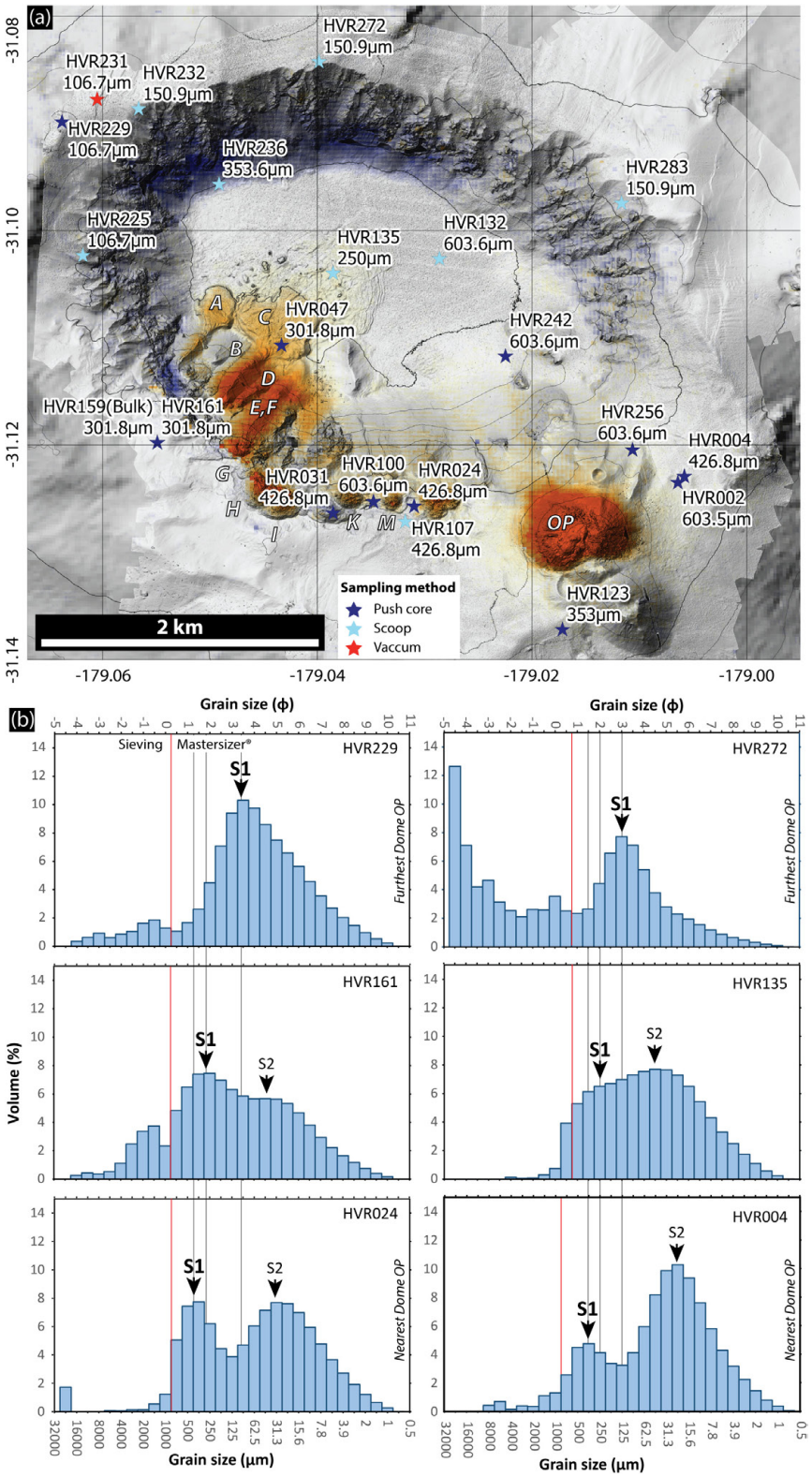

FIGURE 4 | (a) Sample numbers and grainsize peaks for samples of the AL unit from 0.25 φ (~240 µm) and 3.5 φ (~88 µ), inferred to represent S1, across the Havre caldera. **(b)** Representative grain size distributions for samples of the AL unit, with samples closest to Dome OP at the bottom and samples farthest away at the top. The dark lines on the graphs show the location of the inferred S1 peak in each sample for comparison across the caldera. Note the lack of the 5–6 φ mode on the northern caldera rim in samples HVR229 and HVR272.

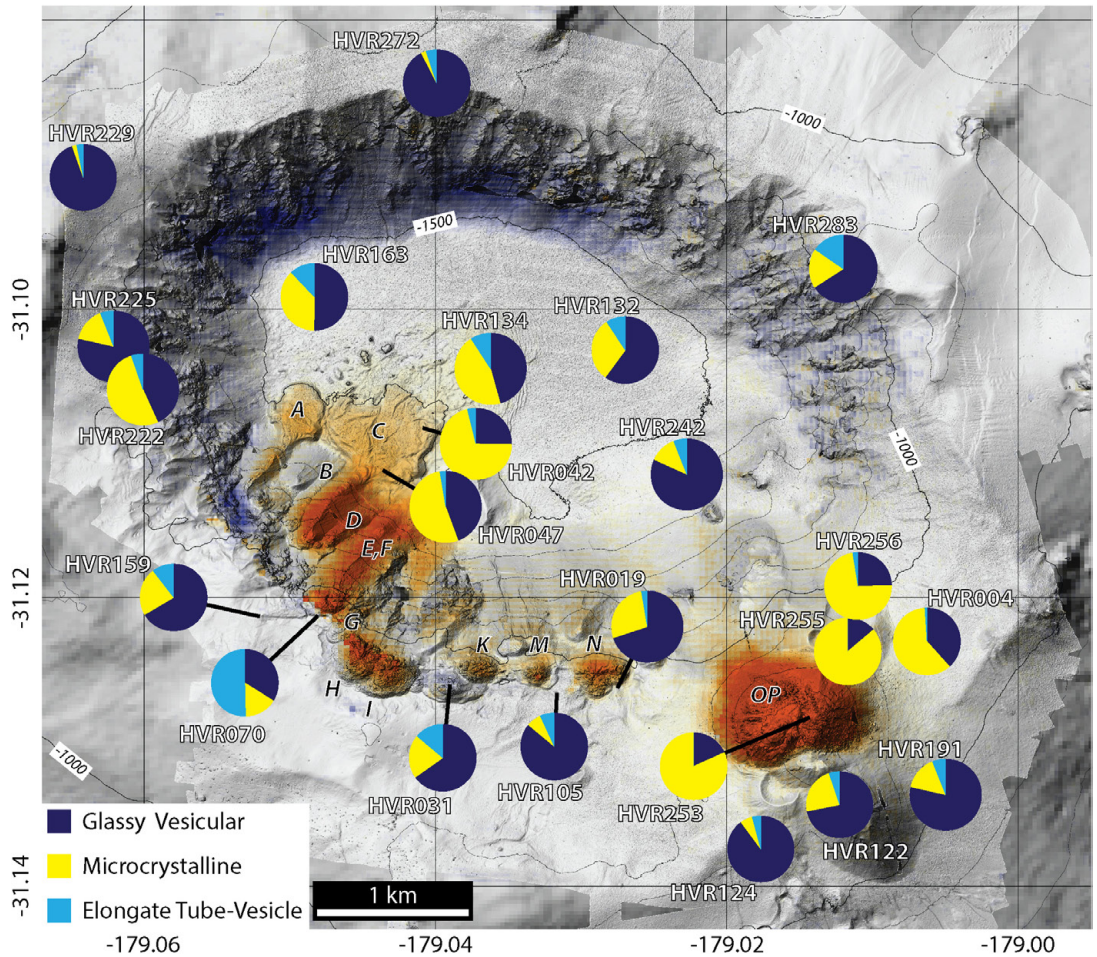

FIGURE 5 | Spatial distribution of componentry data plotted by sample location. Note concentrations in elongate tube-vesicle particles (light blue) around Lava G. Microcrystalline particles (yellow) concentrations are present around Dome OP and the lava flows A–E on the southwest caldera wall, and caldera floor. Glassy vesicular particles (dark blue) are found in every sample and are the dominant component of the overall deposit. Several samples are offset from their sampling location, denoted with a black-tie line.

on the southern, eastern, and western caldera rims. Subunit 2 particles are characterized by their consistent 6–5 φ modal grainsize. Subunit 2 can be identified in all clastic samples south of a boundary that roughly follows the east–west trend of the northern caldera wall (**Figure 4**). To the south, east, and west, Subunit 2 is present to the edge of the investigated area with no notable change in thickness or grainsize. It is inferred to extend well beyond the area, as does Subunit 1.

Subunit 3

Subunit 3 was observed *in situ* in the HVR159 push core where it had a thickness of ∼3 cm (**Figure 6**). In mixed samples, componentry shows that elongate tube-vesicle particles are a minor fraction (6–15%) of samples taken from the southwest caldera rim, caldera floor, and a single sample taken on the northeast caldera rim (**Figure 5**). The highest concentration of elongate tube-vesicle clasts occurs at HVR070 (50%) where the deposit is approximately 0.5 m thick and comprises ash to coarse lapilli (**Figures 2e**, **5**). A similar-looking but unsampled deposit overlies Lava G (**Figure 2f**). Three samples taken south of Dome OP contain 4–6% of these clasts (**Figure 5**). The granulometry and componentry of mixed samples indicate fining of elongate tube-vesicle clasts away from Lava G. This can be seen as a decrease in modal elongate tube-vesicle clasts from larger than −2 φ (4 mm) in HVR070 (nearest sample to Lava G) to smaller than 2 φ (0.25 mm) in HVR283 (4 km from Lava G). A general fining trend in elongate tube-vesicle clasts away from Lava G is also observed through samples HVR031, HVR159, HVR163, and HVR132.

Subunit 4

Subunit 4 is a ∼2 cm thick layer (**Figure 6**) observed on the seafloor at locations HVR132, and HVR163, and in push core HVR159. Microcrystalline grains characterize Subunit 4, and these are found in samples from two separate areas (**Figure 5**). A western area trends northeast across the caldera floor from the southwest caldera rim and is denoted S4w (**Figure 5**). An eastern area, S4e, with microcrystalline particles is around Dome

TABLE 1 | Summary table of subunit dispersal, stratigraphic, and depositional characteristics.

Subunit	Dispersal	Stratigraphic relations	Depositional characteristics	Grainsize/componentry characteristics
S1	• Entire study area.	• Basal contact not seen. Overlies the GP unit. • Relation to the ALB unit unknown.	• At least 5 cm thick at all sites observed. • Drapes topography with no thinning or thickening. • No internal sedimentary features observed.	• Grain size of 0.5–3.5 φ. • Composed of glassy vesicular ash. • No lithic clasts.
S2	• Sharp boundary at the northern caldera wall. South of the boundary deposit extends to the edges of the study area.	• S2 is split in to lower (S2a) and upper (S2b) sections. • Forms current seafloor. Overlies S1 and ALB unit. • S2a has diffusive contact with S1. • S2b overlies domes.	• S2a thickness of ∼2 cm on caldera floor. • Thickness poorly resolved on rim. • S2b on caldera floor 3–14 cm thick vs. ∼2 cm on rim. • Thickest on Lava C (10–14 cm). • Ripples occasionally observed on upper surface (seafloor). • Appears to drape GP clasts to some degree. • No internal sedimentary features observed.	• Characteristic grain size of 6 φ. • Composed of glassy vesicular ash. • No lithic clasts.
S3	• Deposit extends NE–SW across the caldera with boundaries approximately at either caldera wall.	• In proximal locations overlies S2a. • Distally a diffusive layer at the top of S2a.	• Thickens toward the area of Lava G. • >0.5 m thick at HVR070. • Diffusive layer of unknown thickness at HVR283 (most distal). • S3 deposited on topography ∼50 m higher than Lava G. • Topography has little influence on grain size or thickness. • S3 drape topography. • No internal sedimentary features observed.	• Maximum grain size drops from >70 mm on Lava G to <250 μm at HVR283 (most distal). • Characterized by elongate tube-vesicle particles. • No lithic clasts.
S4a	• Deposit extends NE–SW across the caldera. • Thins toward the NE.	• Overlies S3. • Overlain by S2b. • Sharp boundary with S3 and S2b.	• Subunit ∼2 cm thick on the caldera floor (HVR132 and 163) and on the SW rim (HVR159). • Topography does not appear to affect thickness. • S4 drapes topography.	• Characterized by microcrystalline ash. • No lithic clasts.
S4b	• Surrounds Dome OP and extends toward the north down slope.	• Overlies the ALB unit.	• Visually the deposit appears to thin away from Dome OP. • Deposit elongated downslope to the north. • Deposit poorly observed.	• Meter scale blocks proximal to Dome OP. • Maximum grainsize reduces away from Dome OP. • Characterized by microcrystalline ash. • No lithic clasts.

OP (**Figure 5**). All seafloor observations of Subunit 4 were made in the western S4w area (**Figure 5**). There are no apparent differences between clasts of S4w and S4e (**Figure 5**).

Limitations

The stratigraphic framework presented above (**Figure 6**) represents a best estimate from the available data, but we recognize significant potential sources of error. Our ROV sampling techniques did not generally preserve layering, and did not always produce a surface that would allow visual observations of layering. Sampling of the AL unit was also restricted to the proximal depositional areas studied. Despite these limitations, the combination of ROV observations, key samples with preserved layering, and distinctive particle populations give us confidence that the proposed subunits and their mapped distributions adequately represent the seafloor deposits.

Grain Morphology

Glassy vesicular, elongate tube-vesicle, and microcrystalline particles are split into subclasses based on morphology or vesicle form. Glassy vesicular grains show three subclasses; curvi-planar, angular, and fluidal particles (**Figures 3c**, **7**). Curvi-planar clasts are defined by planar and curvi-planar surfaces that intersect to form sharp edges (**Figures 3c**, **7a–c**) and include both platy and sub-equant blocky clasts. Vesicles in curvi-planar clasts are cross-cut by fracture surfaces, which show no deformation around the bubble (**Figure 7a**). Angular clasts have prominent concavities

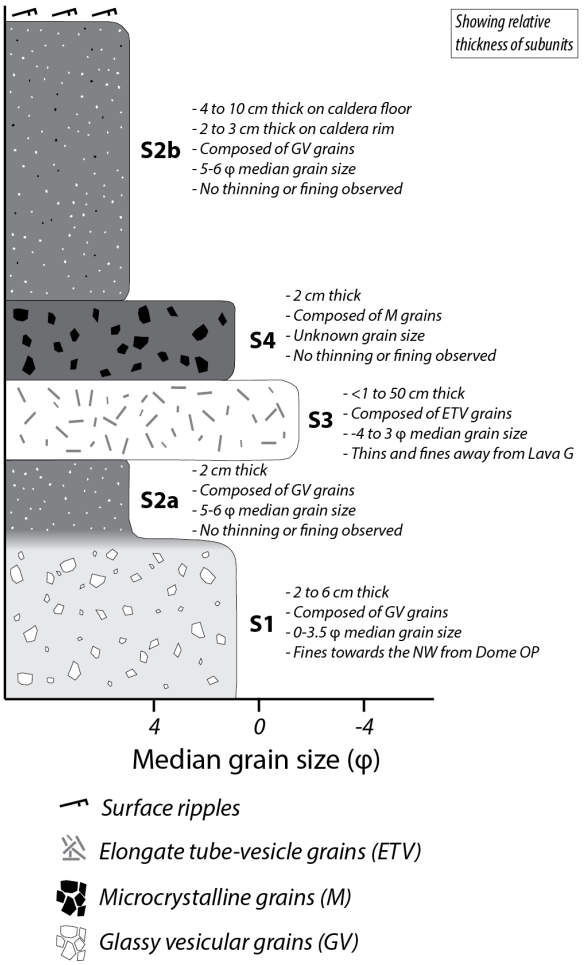

FIGURE 6 | Idealized schematic stratigraphic column of the AL unit showing S1, S2 (a and b), S3, and S4, noting deposit characteristics.

defined by brittle-fractured vesicle walls (**Figures 3e**, **7d–f**). Fluidal clasts have exterior features indicating surface-tension or fluid-dynamic reshaping of the grains while molten. Fluidal clasts include both those with a wholly fluidal form, and those that preserve a single fluidal surface (**Figures 3c**, **7g,h**). Fluidal particles are often cross cut by undeformed curvi-planar fracture surfaces (**Figures 7g,h**).

Microcrystalline particles, by contrast, show only two subclasses; curvi-planar and angular grains (**Figure 3c**). Curvi-planar clasts are typically weakly- to non-vesicular, defined by planar and curvi-planar surfaces that intersect to form sharp edges and include both platy and sub-equant blocky clasts (**Figure 3c**). Angular clasts generally show moderate-vesicularity, with vesicle walls producing complex particle shapes (**Figure 3c**).

Elongate-tube particles are categorized into three different subclasses; elongate tube-angular, elongate tube-ribbed, and elongate tube-fluidal (**Figures 7j–l**). Elongate-tube angular particles are elongate with concave surfaces defined by brittle-fractured bubble walls (**Figure 7j**). Elongate-tube ribbed grains show surface ribs that run parallel to the vesicle and clast elongation direction (inferred to be outer tube-vesicle walls) (**Figure 7k**). The surface ribs have smoothly undulating surfaces and are typically unmarked by vesicles. Elongate tube-fluidal particles have flowing, molten, surfaces on which peaks or droplet-like features are present; they show evidence of ductile necking (**Figure 7l**).

SEM SE images were montaged and used to count particles of different shapes for 3 φ (125 μm), 4 φ (63 μm), and smaller than 4 φ (63 μm) fractions in samples containing few or no microcrystalline clasts. Subunits 1 and 2 are composed dominantly of curvi-planar particles smaller than 3 φ (**Figure 8**). These curvi-planar particles make up between 50 and 86% of the total sample, with a relatively consistent abundance in each grainsize fraction (**Figure 8**). Over the same grainsize range, there are between 2 and 45% angular clasts in S1 and S2, showing an increase in abundance with decreasing grainsize; 12% at 3 φ, to 22% for smaller than 4 φ (**Figure 8**). Fluidal clasts make up 3–35% of clasts in S1 and S2, decreasing with particle size from an average of 19% at 3 φ to 7% for smaller than 4 φ (**Figure 8**).

Microtextural Descriptions

Microtextures of AL unit ash from −1 φ (2 mm) particles to those smaller than 4 φ (63 μm) are characterized by distinctive vesicle and microlite textures. In all clast types phenocrysts compose <5% by solid area, generally in 70–300 μm clusters of euhedral plagioclase and pyroxene.

The groundmass of glassy vesicular clasts is >95% glass, with a microlite population of acicular plagioclase and pyroxene (**Figures 9a,b**). Glassy vesicular clasts are typically moderately to highly vesicular and show a wide range of vesicle size populations, textures, and degrees of vesicle deformation. Vesicles are typically sub-round to round in 2D and range in cross-sectional diameter from <6 up to ∼500 μm. Vesicles smaller than 20 μm are typically isolated, while larger vesicles display more-complex shapes resulting from coalescence and bubble interaction. Vesicles in fluidal glassy vesicular clasts exhibit a range of features indicating ductile behavior of the melt during and after fragmentation, such as inflated bubble walls which protrude from outer clast surfaces, and dense rims unbroken by vesicles enclosing highly vesicular clast cores (**Figures 9g–h**). Some fluidal grains also display several domains in single clasts defined by vesicular cores surrounded by a convex dense fluidal rim (**Figure 9h**).

The groundmass of microcrystalline grains contains 8–35% acicular plagioclase, pyroxene, and Fe–Ti oxide microlites, calculated using ImageJ (**Figures 9c,d**). Plagioclase microlites display swallowtail and hopper forms (**Figures 9c,d**). The characteristics and textures of microcrystalline particles differ between grains (**Figures 9c,d**). One grain also shows apparent mingling of two melts of differing microlite populations (**Figure 9d**). There is cristobalite, both vesicle-hosted and groundmass-replacing, in ∼20% of observed microcrystalline clasts. Vesicles in microcrystalline clasts are generally isolated from one another and have ragged forms that result from the interaction of bubble walls with the microlite population (**Figure 9d**).

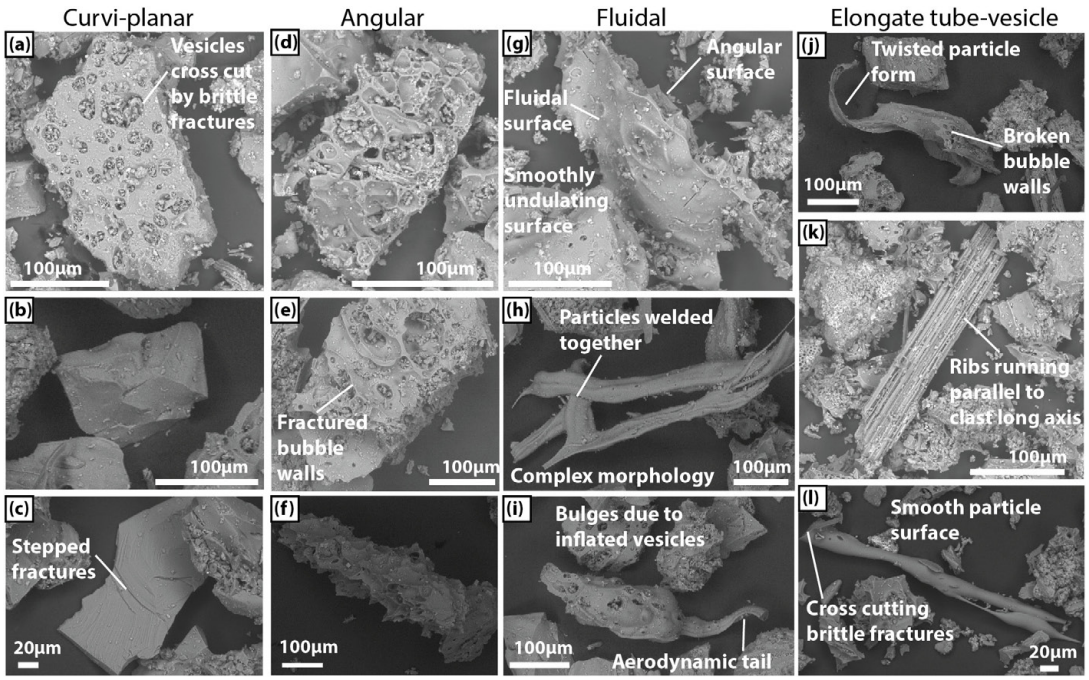

FIGURE 7 | SEM images of representative particles from the different componentry classes; curvi-planar **(a–c)**, angular **(d–f)**, fluidal **(g–i)**, and elongate tube **(j–l)**. In curvi-planar clasts, fracture surfaces cross cut vesicles. Angular particles are bound by fractured vesicle walls with grain morphology dominantly controlled by vesicle texture **(d–f)**. Fluidal particles are defined based on features that are indicative of molten behavior syn/post-fragmentation. This includes ductile reshaping **(g)**, particle welding **(h)**, and post-fragmentation vesicle inflation **(i)**. **(j–l)** Clast-surface textures of elongate tube particles. Note the different scales across images.

Elongate tube-vesicle clasts have >95% groundmass glass with dominantly acicular pyroxene microlites and minor plagioclase (**Figures 9e,f**). Elongate tube-vesicle clasts show generally weak to moderate vesicularity. Vesicles are generally highly elongate, with tube to pipe-like morphologies in 3D and lengths from ∼10 µm to those that traverse the whole length of clasts. The microlites in elongate tube-vesicle clasts are aligned parallel with the vesicle- and clast-elongation direction (**Figures 9e,f**). The smallest vesicles in some particles (<20%) (<10 µm) have circular cross-sectional forms and appear undeformed. Asymmetrical strain shadows can be observed around phenocrysts with vesicles and microlites wrapping around in distinctly flow-like patterns. In the strain shadows vesicles display rounded to sub-rounded forms.

INTERPRETATIONS

Timing, Eruption, and Pyroclast Transport Processes

Subunit 1

Subunit 1 drapes topography, which suggests deposition from suspension in the water column. The wide distribution of this subunit (**Figure 10a**) requires that the height from which the bulk of the grains settled must have been shallower than 700 mbsl, the highest point on the caldera rim. No thinning of Subunit 1 is apparent, but it does fine with distance from Dome OP; we infer that this indicates eruption from a source vent now covered by Dome OP (**Figure 4**). The lack of any apparent internal stratification indicates that the deposition of S1 was broadly continuous (**Figures 2a–d**).

The dominance of glassy vesicular ash in S1 indicates fragmentation of a relatively homogeneous magma (**Figures 3**, **5**). The extremely low microlite content (**Figures 9a,b,g,h**) indicates a high degree of magma undercooling. The modal grainsize of S1, 0.5–3.5 φ (**Figures 4**, **6**) suggests reasonably energetic fragmentation of the magma (Büttner et al., 2002; Zimanowski et al., 2003; Dürig et al., 2012a), while predominant curvi-planar ash morphologies indicate brittle fragmentation (Heiken, 1972; Dürig et al., 2012b; Gonnermann, 2015; Liu et al., 2015; **Figure 8**). Although direct fingerprinting of hydromagmatic fragmentation is difficult (White and Valentine, 2016), the combination of fine particles <0.5 mm across the dispersal area and even proximal to the vent, and the dominance of curvi-planar particles with stepped fractures, points toward magma water interaction-driven fragmentation (e.g., Wohletz, 1983; Büttner et al., 1999, 2002; Austin-Erickson et al., 2008). Fluidal rhyolitic ash grains in S1 (**Figure 7**) indicate that viscous fragmentation mechanisms were also important (Walker and Croasdale, 1971; Porritt et al., 2012). Fluidal ash grains also suggest unusual magma rheology during fragmentation in the Havre eruption. Wholly fluidal clasts cannot have been produced by abrasion from larger particles and must have been produced by a primary volcanic fragmentation mechanism.

Clasts in Subunit 1, the raft pumice, the GP unit, and the ALB unit are all composed of dominantly glassy material with variable vesicle populations and textures (Rotella et al., 2015;

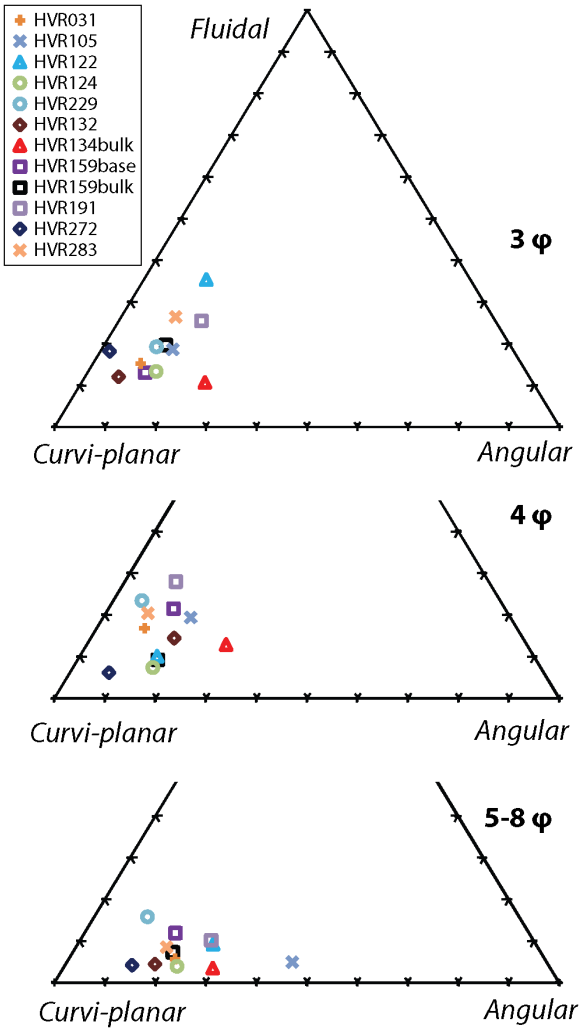

FIGURE 8 | SEM point-count componentry data for 3 φ, 4 φ, and 5–8 φ grainsize fractions. The proportion of fluidal, angular, and curvi-planar particles from natural samples composed dominantly of glassy vesicular clasts (S1 and S2) are shown. Samples show a decrease in the proportion of fluidal ash with decreasing grainsize, and a corresponding increase in angular particles.

Carey et al., 2018; **Figures 9a,b,g,h**), and are distinct from clasts of S3 and S4. Stratigraphically, S1 directly overlies the GP unit, and almost all our seafloor observations of S1 were made from deposits lying on GP clasts. It is not known whether any S1-equivalent ash underlies the GP unit, and the relationship of S1 to the ALB unit is also unknown. The AL unit is much thinner and patchier where it overlies the caldera rim lava domes (**Figures 2g–k**), and there is little or no S1 signature in sample HVR255 (**Figure 5**) from on top of Dome O. These relationships suggest that deposition of S1 began prior to effusion of the caldera rim domes F–O. Given its groundmass microtextural similarities to pumice in the GP unit and raft pumice (Rotella et al., 2015; **Figure 9**), its position immediately overlying GP (**Figure 10b**), and observational evidence that it possibly predates domes F–P (**Figures 2g–k**), we infer that Subunit 1 is associated with the eruption phase that produced the raft pumice, synchronous with or subsequent to deposition of the GP unit (Manga et al., 2018; Mitchell et al., 2018). The presence of a discolored water plume associated with the Havre pumice raft in MODIS images (Carey et al., 2014, 2018; Jutzeler et al., 2014) indicates significant quantities of ash in the water column during emplacement of the pumice raft (**Figure 1**).

The S1 deposit is inferred to have formed through settling of ash dispersed over a wide area by a buoyant plume (**Figure 11a**). The eruption that generated the plume is inferred to have occurred from the same vent that produced the pumice raft and the GP unit now below Dome OP. Modal S1 grains, 500–125 μm, would have settled through 700–1500 m of seawater over 3–52 h if released from the top of the water column (Ferguson and Church, 2004). This settling rate could have been significantly increased through the formation of vertical density currents (e.g., Manville and Wilson, 2004), or somewhat reduced by hindered-settling effects (Druitt, 1995). To produce the observed stratigraphic relationship of S1 overlying GP clasts, we suggest that S1 and the GP deposits were generated during distinct events, with intervening time sufficient that settling produced the GP deposit before deposition of S1 began (**Figure 11a**). Particle morphology of S1 ash grains is inconsistent with an origin by abrasion of raft pumice, and the presence of fluidal ash in S1 further suggests that part of the magma was fragmented without direct water contact. Fragmentation to produce S1 ash is thus inferred to have been driven by a range of processes, some "dry," but overall mostly driven by direct magma–water interaction, and most probably at the same time as the pumice raft was formed.

Subunit 2 (a and b)

Subunit 2 has a well-defined depositional limit along the northern caldera wall and is thicker on the caldera floor than on the caldera rim (**Figure 10**), indicating a strong topographic control on its deposition. Subunit 2 shows no internal stratification or grading, indicating continuous deposition (**Figures 2a–c**). The lack of S2 deposits on the northern caldera rim suggests that S2 ash was erupted from a vent on the southern caldera rim. The extremely fine modal grainsize of S2 would result in particle settling times of ∼1–3 months in still water (Ferguson and Church, 2004) from a height of 500 m above the depositional surface (the height of the caldera walls), though the formation of vertical density currents (e.g., Fiske et al., 1998; Manville and Wilson, 2004) or particle aggregation (Wiesner et al., 1995) could have increased the rate of deposition. The presence of S3 and S4 as discrete layers within S2 is consistent with an inference of prolonged S2 deposition (**Figure 10b**).

Subunit 2 is composed of glassy vesicular ash, indicating fragmentation of a highly undercooled broadly homogeneous magma. The modal grainsize of 6–5 φ indicates highly energetic fragmentation (Büttner et al., 2002; Zimanowski et al., 2003; Dürig et al., 2012a).

Like those of S1, S2 ash grains are broadly similar in groundmass microtexture to the raft pumice (Rotella et al., 2015), the GP unit blocks, and particles of the ALB unit. All comprise dominantly glassy material with varied vesicle populations and

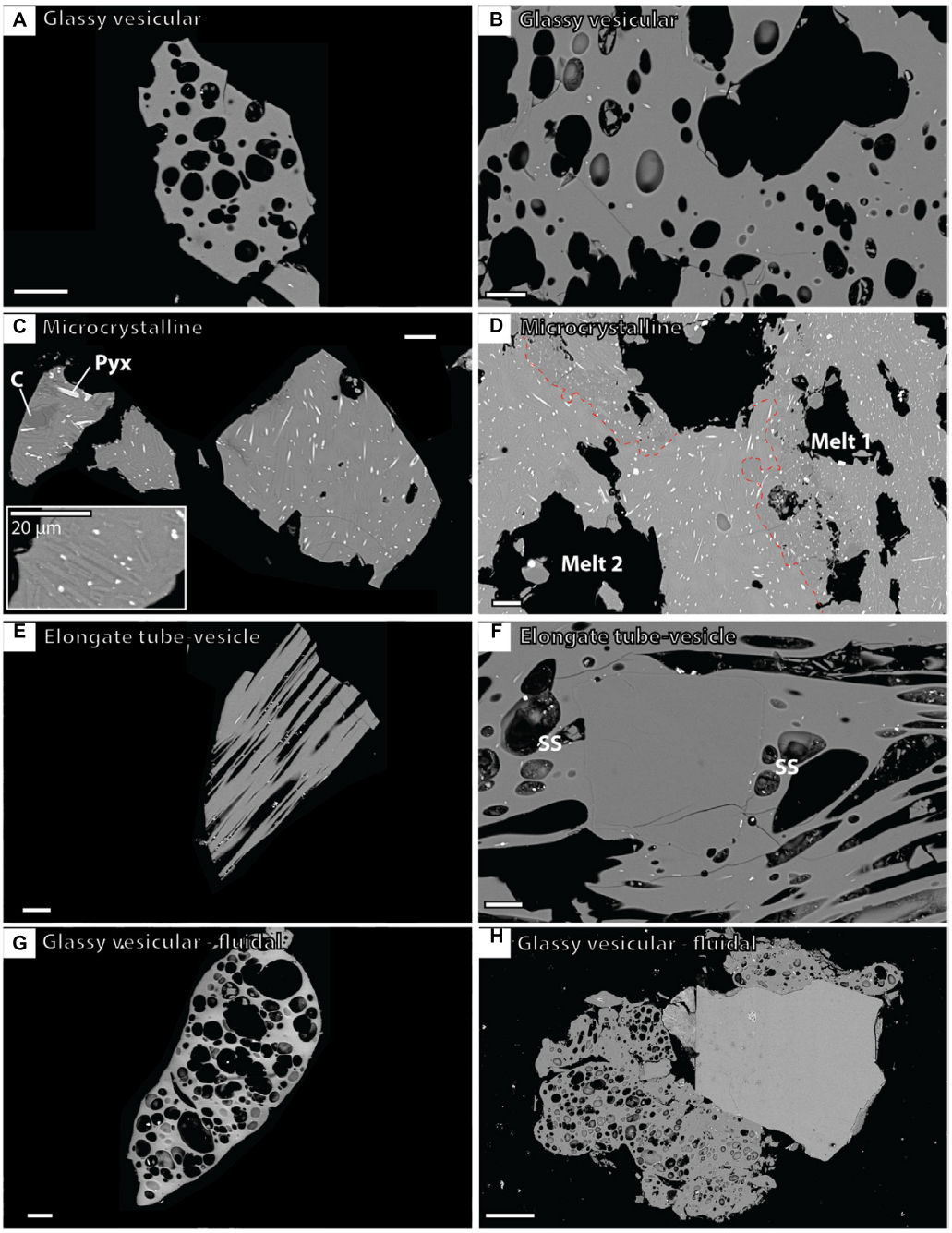

FIGURE 9 | SEM images illustrating representative microtextures of glassy vesicular **(a,b)**, microcrystalline **(c,d)**, elongate tube-vesicle **(e,f)**, and glassy vesicular fluidal **(g,h)** components (scale bars are 100 μm unless otherwise noted). Glassy vesicular particles show rounded vesicles and dominantly glassy groundmasses. Microcrystalline particles show a range of both groundmass crystallinity and vesicle textures **(c,d)**, in **(c)** three microcrystalline grains can be observed each showing differing crystallinities show plagioclase (Plg) and pyroxene (Pyx) microlites. Groundmass-hosted cristobalite (C) is common **(c)**, textures of mingling between melt of different crystallinities are rarely observed **(d)**. Elongate tube-vesicle grains are generally glassy with aligned sheared vesicles and microlites **(e,f)**. Around phenocrysts strain shadows (SS) can occasionally be observed **(f)**. The fluidal particles show a Pele's Tear-like structure with a highly vesicular core and a dense glassy rim **(g,h)**. In the case of **(h)** the Pele's Tear structure appears domainal with several separate vesicular cores and dense rims.

textures. Subunit 2 overlies S1 across a gradational contact (**Figures 2a–c**), suggesting continuous deposition; we infer that S1 and S2 are probably both deposits from the same eruptive event.

Subunit 2 is inferred to have been emplaced from an extremely dilute suspension flow, shed from the same eruption column from which S1 was dispersed (**Figure 11a**). The flow spread radially from an eruption column fed by the vent

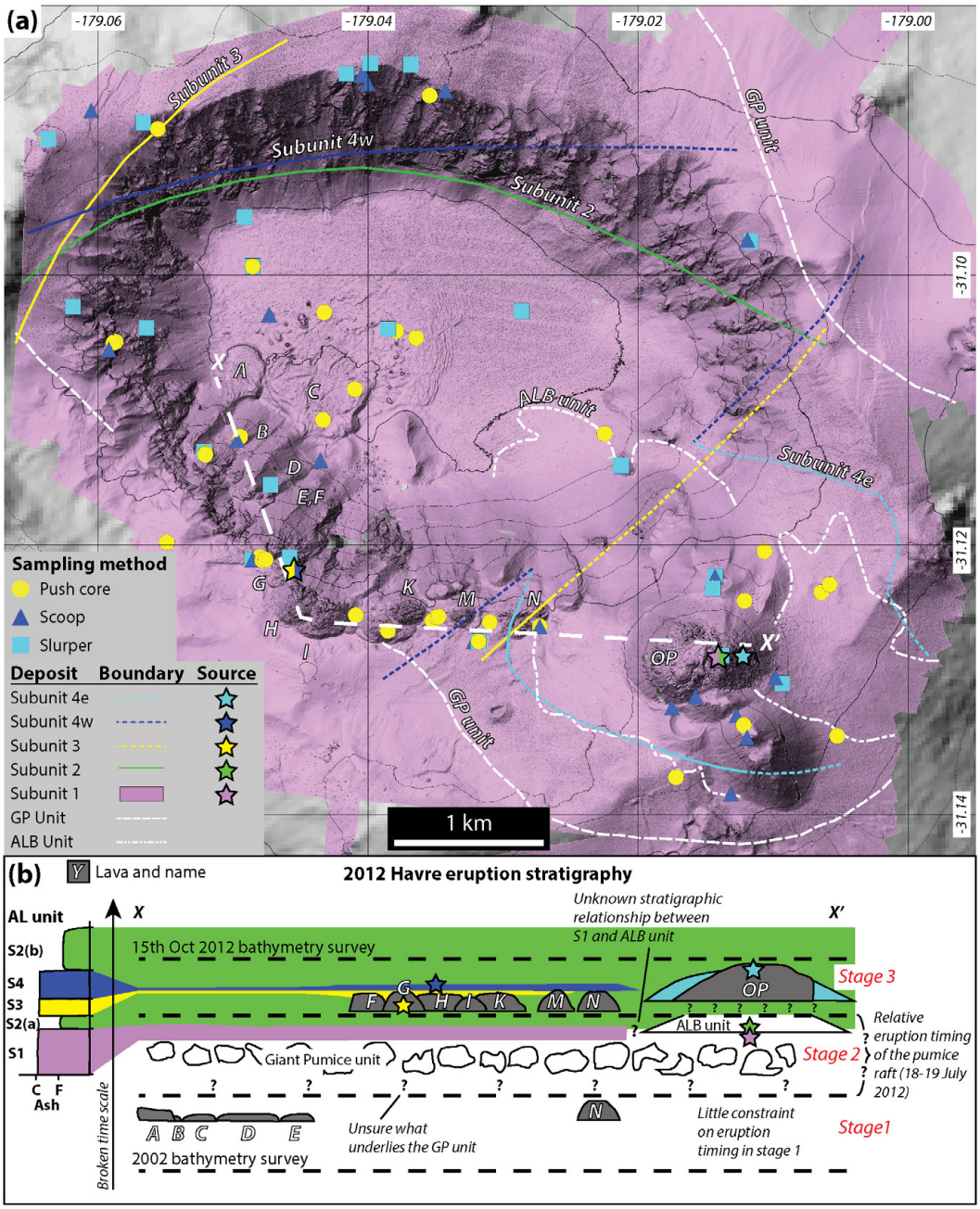

FIGURE 10 | (a) Bathymetric map showing Havre caldera along with the distributions/outlines of the clastic deposits produced during the 2012 Havre eruption where: GP unit – white dashed, ALB unit – white dash and dots, S2 – green, S3 – yellow, S4w – dark blue, and S4e – light blue. Solid line indicates a deposit boundary constrained by sample characteristics, while the dashed boundary are constrained by bathymetry, seafloor texture, etc. Subunit 1 (purple) is present at all sample sites with no change in thickness or grainsize, and is interpreted to extend well beyond AUV-mapped area. The inferred locations of the sources for each subunit are denoted by stars. **(b)** An idealized stratigraphic cross section through the Havre eruption deposits [generalized location shown on **(a)**] showing temporal and spatial relations of deposits from various vents. Three stages have been identified for the Havre eruption reflecting changes in style and location, from dispersed effusive to fragmental eruption focused on a single vent, then to dispersed effusive with weakly pyroclastic behavior.

now filled with Dome OP. On entering the caldera the flow is inferred to have acted in a similar manner to a density current entering a restricted basin (e.g., Pickering et al., 1992; Edwards et al., 1994; Mulder et al., 2009; Pickering and Hiscott, 2009; Talling et al., 2012). Reflection between steep caldera walls caused the flow to pond, resulting in a thickened deposit of S2 compared with outside the caldera. We infer that S2 comprises more-distal and dilute deposits of density currents that also emplaced the ALB unit (**Figure 10**). Rapid slowing of the flow by condensation of any volatile component and

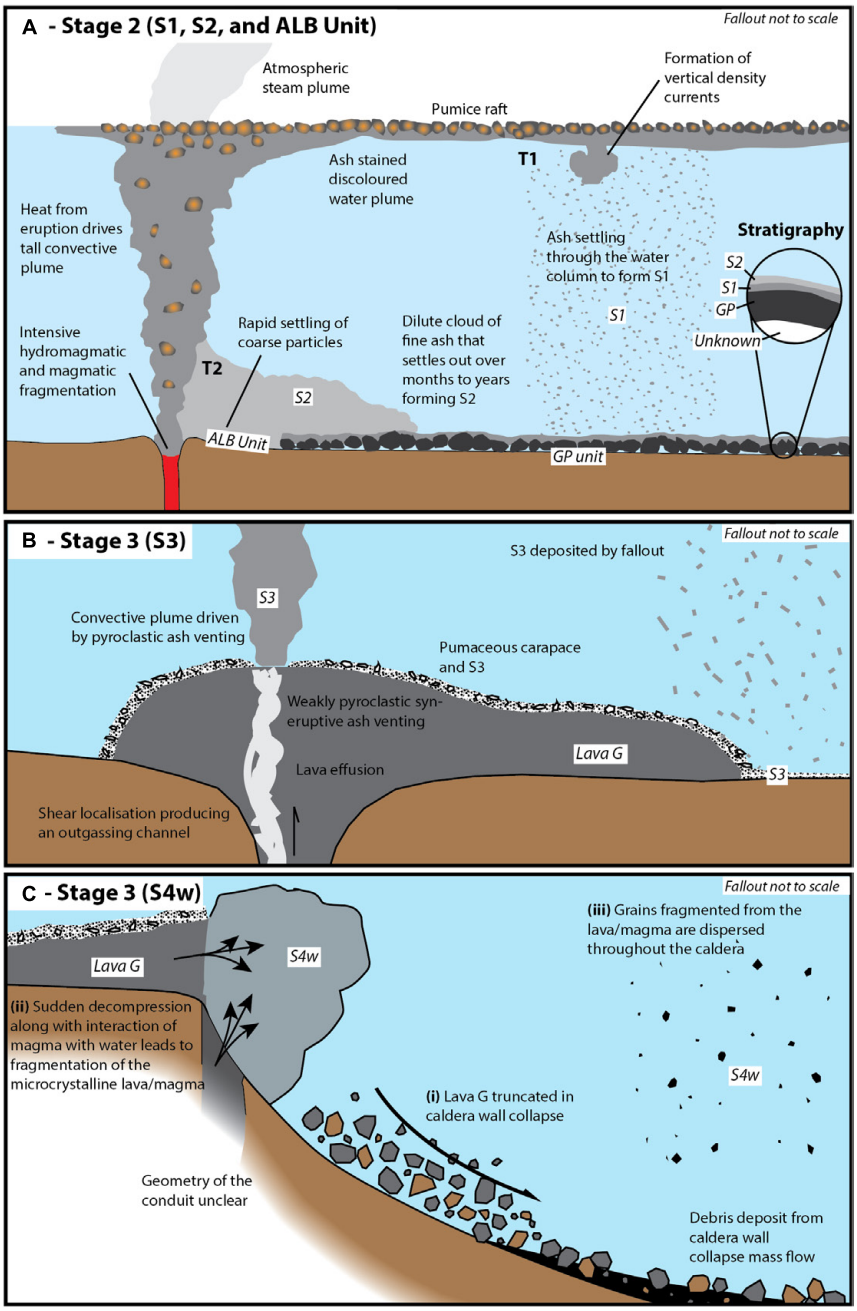

FIGURE 11 | Conceptual model for generation of the various subunits of the seafloor AL unit at Havre. **(a)** Subunits 1 and 2 are inferred to have been formed from the same eruption [at time 1 (T1) and time 2 (T2), respectively], along with the ALB unit and pumice raft. Energetic wet and dry fragmentation of a highly undercooled, ascending, vesiculating magma generated abundant fine particles that were dispersed in an overlying convective column, fallout from which formed S1. Partial or whole-scale collapse of the column, possibility due to vent widening, lead to the formation of density currents. Rapid deposition of the coarse fraction produced the ALB unit surrounding the vent. The remaining dilute flow was then dispersed widely, and from it S2 was deposited. **(b)** Subunit 3 formed during weakly pyroclastic ash venting during the eruption of Lava G. Far-reaching dispersal of the ash occurred in a weak convective column overlying the source of the pyroclastic activity. **(c)** Subunit 4w is inferred to have been formed following caldera wall collapse. Exposure of the hot microcrystalline core of Lava G (+H and I?) to the ambient water resulted in fine-scale fragmentation and dispersal.

friction of the water would result in rapid deposition of coarse suspended material to produce the ALB unit. The deposition of S2 is inferred to have been slow, but the initial generation and injection into the water column of particles was rapid. Over the time during which S2 was being deposited, eruptive activity at the caldera-rim domes and syn-eruptive mass-wasting activity rapidly emplaced S3 and S4, with deposition of S2 continuing afterward (**Figure 10b**).

Subunit 3

Subunit 3 drapes topography, indicating deposition by settling from the water column, and fines and thins away from Lava G (**Figure 10a**). No vent structure is apparent at or near Lava G and we cannot confidently infer a precise source location. The morphological similarity between elongate tube-vesicle clasts that compose S3 and the carapace of Lava G, in addition to S3's thinning and fining trends, suggests that Lava G was the source of S3. Stratigraphically S3 overlies S2a above a gradational contact. Our interpretation is that the deposition of S3 closely followed the eruptive phase that produced the GP deposit, the raft pumice, the ALB, S1, and S2a deposits. Rapid thinning of S3 from ∼0.5 m thick at 150 m distance (HVR070) to 2 cm thick at 900 m distance (HVR159) along with fining away from Lava G suggest a low-intensity eruptive mechanism.

Subunit 3 is composed of elongate tube-vesicle clasts characterized by tube/pipe vesicles (**Figures 7j–l**, **9e,f**). Elongate tube-vesicle clast morphology in S3 indicates both brittle and viscous deformation, before or during fragmentation (**Figures 7j–l**; Heiken, 1972).

The generation of an ash deposit by fallout from a lava flow implies an additional process(es) that drove extensive fragmentation and vertical transport of particles. Viscous fragmentation, as suggested by particle morphology in S3, indicates that fragmentation cannot have been driven by quenching alone, since water contact would rapidly cool the magma preventing viscous deformation. Subunit 3 is therefore inferred to be a fallout deposit produced by weak pyroclastic activity during explosive–effusive effusion of Lava G (**Figure 11b**).

The inference that S3 was generated by explosive–effusive activity implies that Lava G was being actively extruded at the time of S3 deposition (Schipper et al., 2013; Cole et al., 2014; Black et al., 2016). The apparently sharp upper contract of S3 with S4w indicates termination of S3 ash venting prior to onset of S4w deposition.

Transitional explosive–effusive ash venting in subaerial eruptions of silicic magma appears relatively common (e.g., Kennedy and Russell, 2012; Schipper et al., 2013; Cole et al., 2014; Black et al., 2016). The generation of S3 in the deep subaqueous environment would result in modified explosive–effusive behavior, with decreased volatile exsolution due to increased hydrostatic pressure. This would result in a proportional decrease in the depth at which shear induced permeability begins, and a decrease in explosivity. In addition, a reduced magma viscosity, due to decreased exsolution, would result in a greater influence of ductile deformation on permeability development as opposed to brittle fracturing.

Subunit 4w

Subunit 4w occurs both on the caldera rim and caldera floor with microcrystalline clasts apparently concentrated around Lava C on the caldera floor (**Figure 5**). Stratigraphically S4w directly overlies S3 across a sharp boundary (pushcore HVR159; **Figure 3**), and at other sites where S3 is not present overlies 2 cm of S2a (HVR132 and HVR163; **Figures 2a,b**). The sharp basal contact of S4w suggests a rapid onset to deposition at around the same time as production of S3 ceased. Slow inferred accumulation of S2 and its consistent 2 cm thickness below S4w suggest that deposition of S4w began a significant time (weeks?) after the termination of the S2 – forming phase of the Havre eruption.

The microcrystalline clasts that characterize both S4w and S4e were derived from a relatively dense crystalline sources (**Figures 9c,d**). We infer from this that dome-forming lavas had been, or were being, emplaced at the time S4 formed. Deposition of S4w coincided with or followed termination of S3 emplacement (**Figure 11c**). Subunit 4w is most abundant at the base of the southwest caldera and we suggest that S4w formed when partial collapse of the caldera wall truncated Lavas G, H, and I. Evidence for partial caldera wall collapse following the emplacement of Lavas G, H, and I can be seen in the sharp truncation of these lavas along their northern edge by a scallop-shaped scarp (**Figure 1**). The collapse fed a debris avalanche, the deposits of which can be seen in bathymetry of the caldera floor (Carey et al., 2018). We suggest that the collapse permitted water interaction with the hot exposed cores of Lavas G, H, and I, and would have led to MFCI and quench fragmentation (Austin-Erickson et al., 2008), with the particles then deposited from suspension to form S4w.

Subunit 4e

Subunit 4e is present around Dome OP, extends downslope to the north (**Figures 10a**, **11c**) and is composed of microcrystalline clasts. The spatial distribution of S4e indicates a source where Dome OP is located. No thinning or fining trends for S4e could be established. Dispersal is inferred to have been driven by weak sediment-gravity flows. Stratigraphically S4e overlies S1 and S2a, but its relationship to S3 and S4w is uncertain. Microcrystalline particles indicate that S4e was probably generated by fine fragmentation of Dome OP, and we infer that S4e represents the finest-grained fraction of material produced by fragmentation of Dome OP during its emplacement. Meter to decimeter scale blocks cover and extend beyond the slopes of Dome OP and indicate broad fracturing and fragmentation of the lava during extrusion. The exact mechanism driving fine-scale fragmentation in S4e remains unclear.

Eruption and Timing of Havre Depositional Events: Constraints From the AL Unit

Stage 1: The initial phase of the Havre eruption produced Lavas A–E on the caldera floor (**Figure 1**) at some time after the 2002 bathymetric survey of Wright et al. (2006) and prior to the raft pumice phase observed at the sea surface 18–19 July 2012 (Carey et al., 2018; **Figure 10b**). Lavas A–E are inferred to have been emplaced weeks prior to the generation of the pumice raft based on earthquake data (Carey et al., 2018).

Stage 2: Stage 2 includes the pumice raft, GP and ALB units, S1 and S2 subunits (**Figure 10b**). The pumice raft has been inferred to have been generated at the same time as the GP unit was deposited on the seafloor (Carey et al., 2018; Manga et al., 2018). Seafloor stratigraphy indicates that deposition of the

GP unit was followed, first, by deposition of S1 and the ALB. The precise stratigraphic relationship between S1 and ALB is uncertain, but both are overlain by S2a. Based on the similarities in vesicularity, ash shape, and clast groundmass microtextures, we infer that these deposits were erupted from a single vent now beneath Dome OP. The ALB unit, S1, and S2 all overlie the GP deposit, and were probably formed at the time of the pumice raft's generation, ±days depending on the exact eruption mechanics. The deposition of the extremely fine-grained subunit S2a continued for longer because of the extremely slow settling rates of the extremely fine ash.

Stage 3: During late-stage deposition of S2, two ash subunits, S3 and S4, inferred to have been generated during lava effusion were deposited. Both are underlain by S2a. The inferred slow deposition of fine ash in S2a suggests a significant time break between the start of deposition of S2a and the deposition of S3 and S4. The 2 cm of S2a underlying S4w suggests that this time break may have been on the order of weeks. Subunit 3 was generated prior to S4w by ash venting that was probably simultaneous with effusion of lava G. The indication of a time break between the deposition of the ALB unit, S1, and S2 before the generation of S3 during the effusion of lava G is consistent with the observed lack of the AL unit overlying lavas F–O (**Figures 2g–k**). The effusion of lavas F–O is therefore inferred to have occurred days to weeks after the eruption that generated the ALB unit, S1, and S2.

The deposition of S4w resulted from gravitational collapse of the southwest caldera wall around lavas G, H, I. We suggest that the collapse of Lava G in this event terminated S3 deposition. Fine fragmentation to produce S4w is inferred to have occurred through interaction between the hot exposed cores of the lavas and ambient seawater.

Ash Generation During the Raft-Forming Phase

Subunits 1 and 2a overlie a seafloor deposit of giant pumice blocks and are composed of fine ash showing curvi-planar, angular, and fluidal morphologies that indicate a complex fragmentation environment. Ash grainsize and shape data from S1 and S2 point to energetic fragmentation (Büttner et al., 2002; Zimanowski et al., 2003; Dürig et al., 2012a) driven dominantly by direct interaction of magma with water (e.g., Wohletz, 1983; Büttner et al., 1999, 2002; Austin-Erickson et al., 2008; **Figures 3**, **4**), but with an important component of ash having fluidal surfaces that suggest primary hot-state fragmentation of magma isolated from direct water contact (Walker and Croasdale, 1971; Porritt et al., 2012). These inferences point toward the formation of S1 and S2 in an eruption with explosive fragmentation of a highly undercooled vesiculating magma. This eruption generated a vapor-rich eruptive jet and high convective plume from which dilute density currents were generated.

An effusive eruption style unique to the subaqueous environment has previously been inferred for the eruption of the pumice raft and the seafloor GP unit during the Havre eruption (Manga et al., 2018). The presence of S1 and S2 and evidence of their association with the pumice raft presented here indicate that the eruption mechanism presented by Manga et al. (2018) needs to be expanded or modified to include explosive ash generation through both magma–water interaction and dry fragmentation. Ash generation through magma–water interaction may be compatible with the model proposed by Manga et al. (2018); the model's strain-induced fracturing of melt could provide conditions for induced fuel-coolant fragmentation (Austin-Erickson et al., 2008). The fluidal ash grains require a different process.

Limitations on Estimating the Volume of the Ash and Lapilli Unit

The stratigraphy of the AL unit presented in **Figure 10** represents the intra-caldera and near-caldera deposits, but all ash subunits described here extend beyond the study area in one direction or another. A volume of <0.1 km^3 was presented by Carey et al. (2018) for the AL unit within the 35 km^2 study area. There is no evidence of thinning in S1, S2, or even S4w, suggesting that these deposits extend well beyond the study area. Whole-deposit volumes are notoriously difficult to estimate even for comparatively well-understood subaerial dispersal systems (Bonadonna et al., 2015, 2016), and depend critically on treatment of the distal deposits for which we have no information at Havre. The ash component of the 2012 Havre eruption may represent a quite significant component of the overall eruptive volume. The plume of discolored water observed in MODIS imagery on 18–19 July 2012 (Carey et al., 2014, 2018; Jutzeler et al., 2014) also points to a significant population of fines that were carried away from the volcano.

Broader Implications

The 2012 Havre eruption constitutes a key laboratory in the study of large subaqueous silicic eruptions. The results of this study therefore have broader implications both for interpretations of the 2012 Havre eruption, and of other deep subaqueous silicic eruptions. Seafloor products of the 2012 Havre eruption have significant ash in proximal deposits, along with evidence that a substantial population of fines was transported off the volcano. The ash generated during the 2012 Havre constitutes a significant proportion of total fragmental material and represents an even larger proportion of eruptive energy; it must be accounted for in future eruption models.

Ancient subaqueous deposits often appear fines-poor, with ash forming only a minor component (Allen and McPhie, 2000; Kano, 2003; Raos and McPhie, 2003; Stewart and McPhie, 2004). Widespread dispersal of ash at Havre even from weakly explosive (e.g., S3) or non-explosive subaqueous eruptive events (e.g., S4e), along with reworking, provides a possible explanation for the observed lack of thick fines in ancient subaqueous proximal deposits.

A range of ash morphologies are observed in S1 and S2 produced by the higher intensity eruptive phase during which the 18–19 July 2012 pumice raft was generated. These ash morphologies display signatures of both phreatomagmatic and magmatic fragmentation processes during the same eruptive phase. This indicates a spatially and temporally varied

fragmentation environment for S1 and S2, and such variability may be typical of intense silicic eruptions in subaqueous environments.

CONCLUSION

Characteristics of the AL unit presented here constrain our interpretation of the 2012 Havre eruption. The ash-dominated AL unit comprises four subunits. The subunits were generated by different eruptive processes from three locations. Ash particles of subunits S1 and S2 formed from a highly undercooled vesiculating magma. Subunit S1 overlies a seafloor deposit of giant pumice blocks and contains curvi-planar, angular, and fluidal particles indicating a complex fragmentation environment, from which water was excluded from places or at some times. Subunit 2, an extremely fine ash (6–5 phi) records highly effective fragmentation, with particles taking weeks to settle from the water column. Before 2 deposition was complete, lavas F–O were erupted and ash was generated first by ash venting from a vent also responsible for Lava G (S3), and then by interaction between the exposed hot lava and seawater (S4w) following gravitational collapse of the caldera wall, and related to the mass wasting event itself. At about the same time, S4e was dispersed around Dome OP and down into the caldera, probably as the result of extrusion, brecciation, and/or syn–post-eruption reworking.

More broadly, we find that these ash deposits provide information critical to reconstruction of the eruption sequence and processes. This suggests a way to strengthen work on modern submarine volcanoes, at which ash is systematically under-collected by dredging operations, and studies of ancient centers, where typical studies of the proximal deposits neglect detailed work on ash to focus on coherent rocks and breccias.

AUTHOR CONTRIBUTIONS

RC organized and led the cruise. All authors were present on the 2015 cruise and collected the samples. JW established the scope of the project. All sample analysis was conducted by AM. AM drafted the manuscript and produced all figures. All authors read through drafts and assisted in writing the final manuscript.

FUNDING

This research was funded by Australian Research Council Postdoctoral fellowships (DP110102196 and DE150101190 to RC), a short-term postdoctoral fellowship grant from the Japan Society for the Promotion of Science (to RC), National Science Foundation grants (OCE1357443 to BH, OCE1357216), and a New Zealand Marsden grant (U001616 to JW). JW and AM were supported by a research grant, Ph.D. scholarship, and postgraduate publishing bursary from the University of Otago.

ACKNOWLEDGMENTS

We thank the captain, operations teams, marine technicians, and crew of the R/V Roger Revelle for their expert help at sea. We thank the operations team of the ROV Jason and the AUV Sentry. This manuscript contains material included in the Ph.D. thesis of APM (Murch, 2018). Final revisions were completed while AM was supported by a NZ Marsden fund grant to JW.

SUPPLEMENTARY MATERIAL

The Supplementary Material for this article can be found online at: https://www.frontiersin.org/articles/10.3389/feart.2019.00001/full#supplementary-material

REFERENCES

Allen, S. R., and McPhie, J. (2000). Water-settling and resedimentation of submarine rhyolitic pumice at Yali, eastern Aegean, Greece. *J. Volcanol. Geotherm. Res.* 95, 285–307. doi: 10.1016/S0377-0273(99)00127-4

Allen, S. R., and McPhie, J. (2009). Products of neptunian eruptions. *Geology* 37, 639–642. doi: 10.1130/G30007A.1

Allen, S. R., and Stewart, A. J. (2003). "Products of explosive subaqueous felsic eruptions based on examples from the Hellenic Island Arc, Greece," in *Explosive Subaqueous Volcanism: Geophysical Monograph Series*, Vol. 140, eds J. D. L. White, J. L. Smellie, and D. A. Clague (Washington, DC: The American Geophysical Union), 285–298 doi: 10.1029/140GM19

Austin-Erickson, A., Büttner, R., Dellino, P., Ort, M. H., and Zimanowski, B. (2008). Phreatomagmatic explosions of rhyolitic magma: experimental and field evidence. *J. Geophys. Res.* 113:11201. doi: 10.1029/2008JB005731

Black, B. A., Manga, M., and Andrews, B. (2016). Ash production and dispersal from sustained low-intensity mono-inyo eruptions. *Bull. Volcanol.* 78:57. doi: 10.1007/s00445-016-1053-0

Blott, S. J., and Pye, K. (2001). Gradistat: a grain size distribution and statistics package for the analysis of unconsolidated sediments. *Earth Surf. Process. Landf.* 26, 1237–1248. doi: 10.1002/esp.261

Bonadonna, C., Biass, S., and Costa, A. (2015). Physical characterization of explosive volcanic eruptions based on tephra deposits: propagation of uncertainties and sensitivity analysis. *J. Volcanol. Geotherm. Res.* 296, 80–100. doi: 10.1016/j.jvolgeores.2015.03.009

Bonadonna, C., Cioni, R., Costa, A., Druitt, T., Phillips, J., Pioli, L., et al. (2016). MeMoVolc report on classification and dynamics of volcanic explosive eruptions. *Bull. Volcanol.* 78:84. doi: 10.1007/s00445-016-1071-y

Busby-Spera, C. J. (1986). Depositional features of rhyolitic and andesitic volcaniclastic rocks of the mineral king submarine caldera complex, Sierra Nevada, California. *J. Volcanol. Geotherm. Res.* 27, 43–76. doi: 10.1016/0377-0273(86)90080-6

Büttner, R., Dellino, P., La Volpe, L., Lorenz, V., and Zimanowski, B. (2002). Thermohydraulic explosions in phreatomagmatic eruptions as evidenced by the comparison between pyroclasts and products from molten fuel coolant interaction experiments. *J. Geophys. Res. Solid Earth* 107, 1–14. doi: 10.1029/2001JB000511

Büttner, R., Dellino, P., and Zimanowski, B. (1999). Identifying magma–water interaction from the surface features of ash particles. *Nature* 401, 688–690. doi: 10.1038/44364

Carey, R., Soule, S. A., Manga, M., White, J., McPhie, J., Wysoczanski, R., et al. (2018). The largest deep ocean silicic volcanic eruption of the past century. *Sci. Adv.* 4:e1701121. doi: 10.1126/sciadv.1701121

Carey, R. J., Wysoczanski, R., Wunderman, R., and Jutzeler, M. (2014). Discovery of the largest historic silicic submarine eruption. *EOS Trans. AGU* 95, 157–159. doi: 10.1002/2014EO190001

Carlisle, D. (1963). Pillow breccias and their aquagene Tuffs, Quadra Island, British Columbia. *J. Geol.* 71, 48–71. doi: 10.1086/626875

Cas, R. (1978). Silicic lavas in Paleozoic flyschlike deposits in New South Wales, Australia: behavior of deep subaqueous silicic flow. *Geol. Soc. Am. Bull.* 89, 1708–1714. doi: 10.1130/0016-7606(1978)89<1708:SLIPFD>2.0.CO;2

Cas, R. A. F., and Giordano, G. (2014). Submarine volcanism: a review of the constraints, processes and products, and relevance to the Cabo de Gata volcanic succession. *Ital. J. Geosci.* 133, 362–377. doi: 10.3301/IJG.2014.46

Cas, R. A. F., Yamagishi, H., Moore, L., and Scutter, C. (2003). Miocene submarine fire fountain deposits, Ryugazaki Headland, Oshoro Peninsula, Hokkaido, Japan: implications for submarine fountain dynamics and fragmentation processes. *Explosive Subaqueous Volcanism*, eds J. D. L. White, J. L. Smellie, and D. A. Clague (Washington, DC: The American Geophysical Union) 299–316.

Cole, P. D., Smith, P., Komorowski, J.-C., Alfano, F., Bonadonna, C., Stinton, A., et al. (2014). Ash venting occurring both prior to and during lava extrusion at Soufriere Hills Volcano, Montserrat, from 2005 to 2010. *Geol. Soc. London Mem.* 39, 71–92. doi: 10.1144/M39.4

Dimroth, E., and Demarcke, J. (1978). Petrography and mechanism of eruption of the archean dalembert tuff, Rouyn-Noranda, Quebec, Canada. *Can. J. Earth Sci.* 15, 1712–1723. doi: 10.1139/e78-181

Dimroth, E., and Yamagishi, H. (1987). Criteria for recognition of ancient subaqueous pyroclastic rocks. *Geol. Surv. Hokkaido* 58, 55–88.

Dingwell, D. B., and Webb, S. L. (1990). Relaxation in silicate melts. *Eur. J. Miner.* 2, 427–449. doi: 10.1127/ejm/2/4/0427

Druitt, T. H. (1995). Settling behaviour of concentrated dispersions and some volcanological applications. *J. Volcanol. Geotherm. Res.* 65, 27–39. doi: 10.1016/0377-0273(94)00090-4

Dürig, T., Mele, D., Dellino, P., and Zimanowski, B. (2012a). Comparative analyses of glass fragments from brittle fracture experiments and volcanic ash particles. *Bull. Volcanol.* 74, 691–704. doi: 10.1007/s00445-011-0562-0

Dürig, T., Zimanowski, B., Tobias, D., and Zimanowski, B. (2012b). "Breaking news" on the formation of volcanic ash: fracture dynamics in silicate glass. *Earth Planet. Sci. Lett.* 33, 1–8. doi: 10.1016/j.epsl.2012.05.001

Edwards, D. A., Leeder, M. R., Best, J. L., and Pantin, H. M. (1994). On experimental reflected density currents and the interpretation of certain turbidites. *Sedimentology* 41, 437–461. doi: 10.1111/j.1365-3091.1994.tb02005.x

Ferguson, R. I., and Church, M. (2004). A simple universal equation for grain settling velosity. *J. Sediment. Res.* 74, 933–937. doi: 10.1306/051204740933

Fisher, R. V. (1984). Submarine volcaniclastic rocks. *Geol. Soc. London Spec. Publ.* 16, 5–27. doi: 10.1144/GSL.SP.1984.016.01.02

Fiske, R. S., Cashman, K. V., Shibata, A., and Watanabe, K. (1998). Tephra dispersal from Myojinsho, Japan, during its shallow submarine eruption of 1952-1953. *Bull. Volcanol.* 59, 262–275. doi: 10.1007/s004450050190

Gonnermann, H. M. (2015). Magma fragmentation. *Annu. Rev. Earth Planet. Sci.* 43, 431–458. doi: 10.1146/annurev-earth-060614-105206

Gonnermann, H. M., and Manga, M. (2003). Explosive volcanism may not be an inevitable consequence of magma fragmentation. *Nature* 426, 432–435. doi: 10.1038/nature02138

Head, J. W., and Wilson, L. (2003). Deep submarine pyroclastic eruptions: theory and predicted landforms and deposits. *J. Volcanol. Geotherm. Res.* 121, 155–193. doi: 10.1016/S0377-0273(02)00425-0

Heiken, G. (1972). Morphology and petrography of volcanic ashes. *Bull. Geol. Soc. Am.* 83, 1961–1988. doi: 10.1130/0016-7606(1972)83[1961:MAPOVA]2.0.CO;2

Jutzeler, M., Marsh, R., Carey, R. J., White, J. D. L., Talling, P. J., and Karlstrom, L. (2014). On the fate of pumice rafts formed during the 2012 Havre submarine eruption. *Nat. Commun.* 5:3660. doi: 10.1038/ncomms4660

Jutzeler, M., McPhie, J., and Allen, S. R. (2015). Explosive destruction of a pliocene hot lava dome underwater: dogashima (Japan). *J. Volcanol. Geotherm. Res.* 304, 75–81. doi: 10.1016/j.jvolgeores.2015.08.009

Kano, K. (2003). Subaqueous pumice eruptions and their products: a review. *Geophys. Monogr.* 140, 213–229. doi: 10.1029/140GM14

Kano, K., Yamamoto, T., and Ono, K. (1996). Subaqueous eruption and emplacement of the Shinjima Pumice, Shinjima (Moeshima) Island, Kagoshima Bay, SW Japan. *J. Volcanol. Geotherm. Res.* 71, 187–206. doi: 10.1016/0377-0273(95)00077-1

Kennedy, L. A., and Russell, J. K. (2012). Cataclastic production of volcanic ash at Mount Saint Helens. *Phys. Chem. Earth* 4, 40–49. doi: 10.1016/j.pce.2011.07.052

Kokelaar, P. (1986). Magma-water interations in subaqueous and emergent basaltic volcanism. *Bull. Volcanol.* 48, 275–289. doi: 10.1007/BF01081756

Liu, E. J., Cashman, K. V., Rust, A. C., and Gislason, S. R. (2015). The role of bubbles in generating fine ash during hydromagmatic eruptions. *Geology* 43, 239–242. doi: 10.1130/G36336.1

Manga, M., Fauria, K. E., Lin, C., Mitchell, S. J., Jones, M., Conway, C. E., et al. (2018). The pumice raft-forming 2012 Havre submarine eruption was effusive. *Earth Planet. Sci. Lett.* 489, 49–58. doi: 10.1016/j.epsl.2018.02.025

Manville, V., and Wilson, C. J. N. (2004). Vertical density currents: a review of their potential role in the deposition and interpretation of deep-sea ash layers. *J. Geol. Soc.* 161, 947–958. doi: 10.1144/0016-764903-067

Mitchell, S. J., Mcintosh, I. M., Houghton, B. F., Careyc, R. J., and Sheaa, T. (2018). Dynamics of a powerful deep submarine eruption recorded in H 2 O contents and speciation in rhyolitic glass: the 2012 Havre eruption. *Earth Planet. Sci. Lett.* 494, 135–147. doi: 10.1016/j.epsl.2018.04.053

Mulder, T., Zaragosi, S., Razin, P., Grelaud, C., Lanfumey, V., and Bavoil, F. (2009). A new conceptual model for the deposition process of homogenite: application to a cretaceous megaturbidite of the western Pyrenees (Basque region. SW France). *Sediment. Geol.* 222, 263–273. doi: 10.1016/j.sedgeo.2009.09.013

Murch, A. P. (2018). *Ash Generation in the 2012 Eruption of Havre Volcano, Kermadec Arc: The Largest Deep Subaqueous Eruption of the Last Century*. Dunedin: University of Otago.

Namiki, A., and Manga, M. (2008). Transition between fragmentation and permeable outgassing of low viscosity magmas. *J. Volcanol. Geotherm. Res.* 169, 48–60. doi: 10.1016/j.jvolgeores.2007.07.020

Pickering, K. T., and Hiscott, R. N. (2009). Contained (reflected) turbidity currents from the middle ordovician cloridorme formation, Quebec, Canada: an alternative to the antidune hypothesis. *Deep Turbid Syst.* 32, 89–110. doi: 10.1002/9781444304473.ch7

Pickering, K. T., Underwood, M. B., and Taira, A. (1992). Open-ocean to trench turbidity-current flow in the nankai trough: flow collapse and reflection. *Geology* 20, 1099–1102. doi: 10.1130/0091-7613(1992)020<1099:OOTTTC>2.3.CO;2

Porritt, L. A., Russell, J. K., and Quane, S. L. (2012). Pele's tears and spheres: examples from Kilauea Iki. *Earth Planet. Sci. Lett.* 334, 171–180. doi: 10.1016/j.epsl.2012.03.031

Raos, A. M., and McPhie, J. (2003). The submarine record of a large-scale explosive eruption in the Vanuatu arc: ∼ 1 Ma Efaté pumice formation. *Geophys. Monogr. Ser.* 140, 273–283. doi: 10.1029/140GM18

Rotella, M. D., Wilson, C. J. N., Barker, S. J., Ian Schipper, C., Wright, I. C., and Wysoczanski, R. J. (2015). Dynamics of deep submarine silicic explosive eruptions in the Kermadec arc, as reflected in pumice vesicularity textures. *J. Volcanol. Geotherm. Res.* 301, 314–332. doi: 10.1016/j.jvolgeores.2015.05.021

Rotella, M. D., Wilson, C. J. N., Barker, S. J., and Wright, I. C. (2013). Highly vesicular pumice generated by buoyant detachment of magma in subaqueous volcanism. *Nat. Geosci.* 6, 129–132. doi: 10.1038/ngeo1709

Schipper, C. I., Castro, J. M., Tuffen, H., James, M. R., and How, P. (2013). Shallow vent architecture during hybrid explosive-effusive activity at Cordón Caulle (Chile, 2011-12): evidence from direct observations and pyroclast textures. *J. Volcanol. Geotherm. Res.* 262, 25–37. doi: 10.1016/j.jvolgeores.2013.06.005

Schipper, C. I., White, J. D. L., Houghton, B. F., Shimizu, N., and Stewart, R. B. (2010). "Poseidic" explosive eruptions at Loihi Seamount. Hawaii. *Geology* 38, 291–294. doi: 10.1130/G30351.1

Schmid, A., Sonder, I., Seegelken, R., Zimanowski, B., Büttner, R., Gudmundsson, M. T., et al. (2010). Experiments on the heat discharge at the dynamic magma-water-interface. *Geophys. Res. Lett.* 37, 2–5. doi: 10.1029/2010GL044963

Simpson, K., and McPhie, J. (2001). Fluidal-clast breccia generated by submarine fire fountaining, Trooper Creek Formation, Queensland, Australia. *J. Volcanol. Geotherm. Res.* 109, 339–355. doi: 10.1016/S0377-0273(01)00199-8

Staudigel, H., and Schmincke, H. U. (1984). The Pliocene Seamount Series of La Palma/Canary Islands. *J. Geophys. Res.* 89, 11195–11215. doi: 10.1029/JB089iB13p11195

Stewart, A. L., and McPhie, J. (2004). An upper pliocene coarse pumice breccia generated by a shallow submarine explosive eruption, Milos, Greece. *Bull. Volcanol.* 66, 15–28. doi: 10.1007/s00445-003-0292-z

Talling, P. J., Masson, D. G., Sumner, E. J., and Malgesini, G. (2012). Subaqueous sediment density flows: depositional processes and deposit types. *Sedimentology* 59, 1937–2003. doi: 10.1111/j.1365-3091.2012.01353.x

van Otterloo, J., Cas, R. A. F., and Scutter, C. R. (2015). The fracture behaviour of volcanic glass and relevance to quench fragmentation during formation of hyaloclastite and phreatomagmatism. *Earth Sci. Rev.* 151, 79–116. doi: 10.1016/j.earscirev.2015.10.003

Walker, G. P. L., and Croasdale, R. (1971). Characteristics of some basaltic pyroclastics. *Bull. Volcanol.* 35, 303–317. doi: 10.1007/BF02596957

White, J. D. L., and Houghton, B. F. (2006). Primary volcaniclastic rocks. *Geology* 34, 677–680. doi: 10.1130/G22346.1

White, J. D. L., Schipper, C. I., and Kano, K. (2015). *Submarine Explosive Eruptions*, 2nd Edn. New York, NY: Elsevier Inc. doi: 10.1016/B978-0-12-385938-9.00031-6

White, J. D. L., Smellie, J. L., and Clague, D. A. (2003). "Introduction: a deductive outline and topical overview of subaqueous explosive volcanism," in *Explosive Subaqueous Volcanism*, eds J. D. L. White, J. L. Smellie, and D. A. Clague (Washington, DC: American Geophysical Union).

White, J. D. L., and Valentine, G. A. (2016). Magmatic versus phreatomagmatic fragmentation: absence of evidence is not evidence of absence. *Geosphere* 12, 1478–1488. doi: 10.1130/GES01337.1

Wiesner, M. G., Wang, Y. B., and Zheng, L. F. (1995). Fallout of Volcanic Ash to the deep South China Sea induced by the 1991 eruption of Mount-Pinatubo (Philippines). *Geology* 23, 885–888. doi: 10.1130/0091-76131995023

Wohletz, K. H. (1983). Mechanisms of hydrovolcanic pyroclast formation: grain-size, scanning electron microscopy, and experimental studies. *J. Volcanol. Geotherm. Res.* 17, 31–63. doi: 10.1016/0377-0273(83)90061-6

Wright, I. C., Worthington, T. J., and Gamble, J. A. (2006). New multibeam mapping and geochemistry of the 30°-35° S sector, and overview, of southern Kermadec arc volcanism. *J. Volcanol. Geotherm. Res.* 149, 263–296. doi: 10.1016/j.jvolgeores.2005.03.021

Zimanowski, B., Buttner, R., and Lorenz, V. (1997). Premixing of magma and water in MFCI experiments. *Bull. Volcanol.* 58, 491–495. doi: 10.1007/s004450050157

Zimanowski, B., Wohletz, K., Dellino, P., and Büttner, R. (2003). The volcanic ash problem. *J. Volcanol. Geotherm. Res.* 122, 1–5. doi: 10.1016/S0377-0273(02)00471-7

Conflict of Interest Statement: The authors declare that the research was conducted in the absence of any commercial or financial relationships that could be construed as a potential conflict of interest.